

Predictions for Detecting a Turndown in the Baryonic Tully Fisher Relation

Dilys Ruan,¹★ Alyson M. Brooks,¹ Akaxia Cruz^{2,3}, Annika H. G. Peter^{4,5,6}, Ben Keller⁷, Thomas Quinn⁸, James Wadsley⁹, and Elizabeth A. K. Adams^{10,11}

¹ Department of Physics and Astronomy, Rutgers University, Piscataway, NJ 08854, USA

² Center for Computational Astrophysics, Flatiron Institute, 162 Fifth Avenue, New York, NY 10010, USA

³ Department of Physics, Princeton University, Princeton, NJ 08544, USA

⁴ CCAPP, The Ohio State University, 191 W Woodruff Ave, Columbus, OH 43210

⁵ Department of Physics, The Ohio State University, 191 W Woodruff Ave, Columbus, OH 43210

⁶ Department of Astronomy, The Ohio State University, 140 W 18th Ave, Columbus, OH

⁷ Department of Physics and Materials Science, The University of Memphis, Memphis, TN 38152

⁸ Astronomy Department, University of Washington, Seattle, WA 98195, USA

⁹ Department of Physics and Astronomy, McMaster University, Hamilton, L8S 4M1, Canada

¹⁰ ASTRON, the Netherlands Institute for Radio Astronomy, Oude Hoogetveensedijk 4, 7991 PD Dwingeloo, The Netherlands

¹¹ Kapteyn Astronomical Institute, University of Groningen, PO Box 800, 9700 AV Groningen, The Netherlands

Accepted XXX. Received YYY; in original form ZZZ

ABSTRACT

The baryonic Tully Fisher relationship (bTFR) provides an empirical connection between baryonic mass and dynamical mass (measured by the maximum rotation velocity) for galaxies. Due to the impact of baryonic feedback in the shallower potential wells of dwarf galaxies, the bTFR is predicted to turn down at low masses from the extrapolated power-law relation at high masses. The low-mass end of the bTFR is poorly constrained due to small samples and difficulty in connecting the galaxy’s gas kinematics to its dark matter halo. Simulations can help us understand this connection and interpret observations. We measure the bTFR with 66 dwarf galaxies from the Marvel-ous and Marvelous Massive Dwarfs hydrodynamic simulations. Our sample has $M_{\star} = 10^6 - 10^9 M_{\odot}$, and is mostly gas dominated. We compare five velocity methods: $V_{\text{out,circ}}$ (spatially resolved mass-enclosed), $V_{\text{out,mid}}$ (spatially resolved midplane gravitational potential), and unresolved H I linewidths at different percentages of the peak flux (W_{10} , W_{20} , and W_{50}). We find an intrinsic turndown in the bTFR for maximum halo speeds $\lesssim 50 \text{ km s}^{-1}$ (or total baryonic mass, $M_{\text{bary}} \lesssim 10^{8.5} M_{\odot}$). We find that observing H I in lower-mass galaxies to the conventional surface density limit of $1 M_{\odot} \text{ pc}^{-2}$ is not enough to detect a turndown in the bTFR; none of the H I velocity methods (spatially resolved or unresolved) recover the turndown, and we find bTFR slopes consistent with observations of higher-mass galaxies. However, we predict that the turndown can be recovered by resolved rotation curves if the H I limit is $\lesssim 0.08 M_{\odot} \text{ pc}^{-2}$, which is within the sensitivity of current H I surveys like FEASTS and MHONGOOSE.

Key words: galaxies: dwarf – Galaxy: kinematics and dynamics – Galaxy: evolution

1 INTRODUCTION

Rotation curves provided some of the earliest evidence for dark matter halos (Bosma 1978; Rubin et al. 1980) since rotation velocities trace the dynamical mass. The Tully Fisher Relation (TFR) (Tully & Fisher 1977) is a measurement of galaxy stellar mass (or luminosity) as a function of rotation velocity, and thus provides an empirical constraint between a galaxy’s stellar mass and underlying dark matter halo mass. Similar to the stellar-mass halo-mass (SMHM) relation (e.g., Wechsler & Tinker 2018; Munshi et al. 2021), the TFR helps us understand the galaxy-halo connection and galaxy evolution. Both the TFR and SMHM relation can tell us what fraction of the cosmic baryon abundance has cooled into halos and formed stars. The baryonic Tully Fisher Relation (bTFR) instead connects baryonic mass (M_{bary} , total cold gas + stellar mass) to halo mass (McGaugh et al.

2000). This relation is especially useful to study lower-mass galaxies, in which the baryonic content is dominated by cold gas ($T < 10^4 \text{ K}$) in the atomic hydrogen (HI) phase. Additionally, H I gas extends farther out into the halo than stars, and therefore gives us a better tracer of the underlying halo velocity to be used in the bTFR.

For galaxies with $M_{\text{bary}} \sim 10^8 - 10^{12} M_{\odot}$, baryonic mass and the rotation velocity of gas follow a power-law with a bTFR slope of 3 – 4 (e.g., Lelli et al. 2016b; Bradford et al. 2016; Lelli et al. 2019). The bTFR slope demonstrates a similar scaling between the baryonic disks and dark matter halos of galaxies, despite the many processes which redistribute baryons and dark matter (e.g., Pontzen & Governato 2012; Di Cintio et al. 2014). Scatter in the bTFR tells us how much this scaling differs from galaxy-to-galaxy. Intrinsic scatter in the bTFR is ~ 0.15 dex, and is mostly due to scatter in the mass-concentration relation between halos (Dutton 2012).

For lower-mass galaxies ($M_{\text{bary}} \lesssim 10^8 M_{\odot}$), the bTFR is expected to steepen, or have a ‘turndown’, because baryonic feedback leads to

★ E-mail: druan@physics.rutgers.edu

an overall decrease in star formation efficiency and loss of gas (e.g., Ferrero et al. 2012; Oman et al. 2016). These processes can be internal to the galaxy (e.g., galactic winds resulting from stellar feedback), or these processes can be external (e.g., UV background radiation from post-reionization, which can heat gas and prevent accretion). Hydrodynamic simulations predict a turn-down in the bTFR around a rotation speed of 40 km s^{-1} if the maximum rotation velocities of the dwarf galaxy halos are used (Ferrero et al. 2012; Brook & Shankar 2016; Sales et al. 2017; Trujillo-Gomez et al. 2018; Sardone et al. 2024).

Measuring the bTFR at lower masses is difficult due to limited sample sizes of low-surface brightness galaxies and difficulty in matching gas to halo kinematics. Only a handful of resolved rotation curves have been measured in dwarf galaxies (e.g., Oh et al. 2015). Although H I gas extends farther out in radius than stars (e.g., Krumm & Burstein 1984; Hunter et al. 2016), the H I may not extend far enough to measure the rotation curve at the flat part. Many measurements to date extend out to a radius where the H I surface density drops below $1 \text{ M}_\odot \text{ pc}^{-2}$ (e.g., Broeils & Rhee 1997; Wang et al. 2016). At this limit, some observed rotation curves are ‘still rising’, suggesting that the maximum rotation velocity is not being directly measured. McQuinn et al. (2022) constrained the bTFR with 25 galaxies at $M_{\text{bary}} < 10^8 \text{ M}_\odot$. They used the outermost H I velocities, and found no turn-down in the bTFR. However, using an adopted mass model, they were able to extrapolate the maximum rotation velocities that best matched each of their outermost rotation velocities. Assuming a cored Einasto dark matter density profile, the extrapolated velocities yielded a bTFR turn-down at $\sim 40 \text{ km s}^{-1}$ and baryon fractions of 1-10% of the cosmic value.

Current and upcoming radio surveys such as Apertif (van Cappellen et al. 2022; Adams et al. 2022); FEASTS (FAST Extended Atlas of Selected Targets Survey, Wang et al. 2025); MHONGOOSE (MeerKAT H I Observations of Nearby Galactic Objects: Observing Southern Emitters, de Blok et al. 2024); MIGHTEE-H I (MeerKAT International GigaHertz Tiered Extragalactic Exploration survey - HI, Maddox et al. 2021); and WALLABY (Widefield ASKAP L-band Legacy All-sky Blind survey, Koribalski et al. 2020; Spekkens et al. 2020; Deg et al. 2024) are sensitive down to rotation speeds of $\sim 30\text{--}40 \text{ km s}^{-1}$, below where the bTFR turn-down is expected. However, these resolved rotation curves will still be limited to the nearest dwarf galaxies. The time required to obtain large sample sizes will still be prohibitive. For representative samples, spatially *unresolved* H I velocities are thought to be necessary, since they require less integration time and can be measured by both radio interferometers and single-dish telescopes. Studies with unresolved H I velocities (e.g., Klypin et al. 2015; Lelli et al. 2016b; Bradford et al. 2016) can have about two orders of magnitude more galaxies than spatially resolved observations (e.g., Klypin et al. 2015; Papastergis & Shankar 2016; McQuinn et al. 2022). Sardone et al. (2024) demonstrated that spatially unresolved, high spectral resolution observations are needed to detect the most diffuse gas in the outer wings of the H I profile, and this can reduce bTFR scatter at lower masses.

It is well established that different velocity tracers of the maximum halo speed (V_{max}) exhibit different bTFR slopes. This has been studied in observations (e.g., Verheijen 2001; Bradford et al. 2016; Lelli et al. 2019) and simulations (e.g., Brook et al. 2016; Brooks et al. 2017; Sardone et al. 2024). For spatially unresolved H I velocities, linewidths at 50% (W_{50}) or 20% (W_{20}) of the peak flux emission are reported as proxies for $2V_{\text{max}}$. Higher-mass galaxies have flat rotation curves, and therefore more material with high column densities moving at the same velocity V_{max} . This high-velocity gas leads to a ‘double-horned’ spectral feature that makes W_{50} a

better proxy to $2V_{\text{max}}$. In the case of lower-mass galaxies, where H I rotation curves are still rising and the contribution from non-circular motions is greater, the H I flux profile is more Gaussian, and W_{50} underestimates $2V_{\text{max}}$ (e.g., Brook et al. 2016; Yaryura et al. 2016). W_{20} can provide a more accurate tracer of $2V_{\text{max}}$ than W_{50} (Macciò et al. 2016; Brook & Shankar 2016; Brooks et al. 2017; Dutton et al. 2019; Sardone et al. 2024), though still deviates at lower masses. Although W_{10} (linewidth at 10% of the peak H I flux) is the largest linewidth, and therefore closest to $2V_{\text{max}}$ for dwarf galaxies, it is also susceptible to noise from outer velocity channels.

We utilize the largest suite of simulated dwarf galaxies, with realistic H I content, to understand how the bTFR turn-down might manifest in observations. In this work, we analyze our sample of 66 dwarf galaxies from the Marvel-ous and Marvelous Massive Dwarfs hydrodynamic simulation suites. Our sample consists of isolated galaxies with $M_{\text{HI}} > 10^6 \text{ M}_\odot$, and $M_\star = 10^6 - 10^9 \text{ M}_\odot$. We focus on understanding why H I velocities (spatially resolved or unresolved) do not trace the halo’s V_{max} . We also make predictions about whether the halo’s V_{max} is recoverable with deeper H I observations. In Section 2, we describe the properties and physics implemented in our simulations, and define the velocities and masses used in our study. Section 3 presents our results and demonstrates how velocity definitions and sensitivity limits affect our ability to measure a bTFR turn-down. Section 4 discusses how our bTFR results compare to observations and upcoming H I surveys. Section 5 summarizes our results.

2 SIMULATIONS & METHODS

High resolution “zoom-in” simulations allow us to take a larger volume, identify high-density regions of interest (e.g., a halo of a given mass), and embed higher resolution particles in a smaller region to simulate the star formation and baryonic feedback with better spatial and temporal resolution. The large volume at lower resolution (external to the high-resolution particles) is needed because large-scale structure is responsible for the build-up of angular momentum in the main halo, according to tidal torque theory (Peebles 1969; Barnes & Efstathiou 1987). The zoom-in is run with higher resolution and hydrodynamics for a region on the order of a few virial radii from the main halo’s center.

In this work, we use two smoothed particle hydrodynamics (SPH) + N-body zoom-in simulation sets, the Marvel-ous and Marvelous Massive Dwarfs suites (hereafter, Marvel and Massive Dwarfs, respectively). Marvel (Munshi et al. 2021) is a set of four zoom-in regions that each contain dozens of dwarf galaxies. The simulations are called CptMarvel, Elektra, Rogue, and Storm. The other simulation suite, Massive Dwarfs, consists of zoom-ins of individual halos selected from the Romulus25 simulation (Tremmel et al. 2017), focusing on dwarf galaxies with $M_\star \sim 10^{8-9} \text{ M}_\odot$.

Large-scale structure depends on the input cosmology. The baryon content will also be influenced by the cosmic fraction, which is set by the matter density and baryon density parameters, Ω_m and Ω_b , respectively. We assume Λ CDM and do not consider alternative types of dark matter. Marvel uses a WMAP3 cosmology (Spergel et al. 2007) ($h = 0.732$, $\Omega_m = 0.276$, $\Omega_b h^2 = 0.02229$). Massive Dwarfs uses the same cosmology as Romulus25, which is Planck 2015 (Planck Collaboration et al. 2016) ($h = 0.677$, $\Omega_m = 0.307$, $\Omega_b h^2 = 0.02226$). Since our results mostly depend on the cosmic baryon fraction (WMAP3 with $f_b = 0.1507$ versus Planck 2015 with $f_b = 0.1582$), we do not expect that the different cosmologies will have a significant impact on our results.

Due to the discreteness of particle simulations, forces can only be

resolved to a minimum spatial scale, and each type of particle has a minimum mass. The Marvel simulation has a total low-resolution volume of $(25 \text{ Mpc})^3$ and uses 60 pc for the spline gravitational force resolution, $420 M_\odot$ for initial star particle mass, $1410 M_\odot$ for gas particle mass, and $6650 M_\odot$ for dark matter particle mass. The Massive Dwarfs are run at a higher resolution than Romulus25 (3 times higher force resolution, 512 times higher mass resolution). Each Massive Dwarfs simulation has a volume of $(25 \text{ Mpc})^3$, and uses 87 pc for spline gravitational force resolution, $994 M_\odot$ for initial star particle mass, $3300 M_\odot$ for gas particle mass, and $18000 M_\odot$ for dark matter particle mass.

Our simulations use the code CHANGA (Menon et al. 2015) for the SPH + N-body processes. The hydrodynamics are from GASOLINE2 (Wadsley et al. 2004, 2017), while CHANGA has a faster gravity solver. CHANGA scales well to simulations with a large number of particles due to its implementation in CHARM++ (Kalé & Krishnan 1993), which handles dynamic load balancing and communication for thousands of computing cores.

CHANGA calculates non-equilibrium ion abundances and gas cooling from collisional ionization rates (Abel et al. 1997), radiative recombination (Black 1981; Verner & Ferland 1996), photo-ionization, free-free emission, and cooling from hydrogen and helium (Cen 1992). The heating and cooling rates consider effects from a redshift-dependent, uniform UV background (Haardt & Madau 2012). Our simulations include the non-equilibrium formation, shielding, cooling, and destruction of H_2 , as implemented by Christensen et al. (2012). Metal-line cooling and metal distribution are based on the model of Shen et al. (2010).

We adopt the star formation probability from Stinson et al. (2006) and require the presence of H_2 based on Christensen et al. (2012):

$$p = \frac{m_{\text{gas}}}{m_{\text{star}}} \left(1 - e^{-c_0^* X_{H_2} \Delta t / t_{\text{form}}} \right), \quad (1)$$

where m_{gas} is the gas particle mass, m_{star} is the initial star particle mass, c_0^* is the star formation efficiency parameter (set to 0.1), X_{H_2} is the H_2 fraction of the gas particle, Δt is the time step for star formation in the simulation ($\sim 1 \text{ Myr}$), and t_{form} is the local dynamical time. Star formation is limited to cold gas particles ($T < 1000 \text{ K}$), and a number density $n > 0.1 \text{ cm}^{-3}$ is required. Since we also require the presence of H_2 , star formation usually occurs in much denser gas, so the actual density for star formation is generally $n > 100 \text{ cm}^{-3}$. In both Marvel and Massive Dwarfs, each star particle follows the initial mass function from Kroupa (2001).

Marvel uses blastwave feedback (Stinson et al. 2006), while Massive Dwarfs uses superbubble feedback (Keller et al. 2014). Blastwave feedback injects metals, thermal energy, and mass into gas that is within the blastwave radius of the supernova (SN), as calculated by the blast wave solution for a SN remnant in Ostriker & McKee (1988). The deposited energy is $\sim 1.5 \times 10^{51} \text{ erg per SN}$. To prevent numerical overcooling, blastwave feedback relies on turning off radiative cooling in the surrounding gas, to limit thermal energy loss in supernovae for a time corresponding to the end of the snowplow phase. Superbubble feedback does not disable radiative cooling, but instead puts feedback-heated particles into a temporary two-phase state, with each phase cooling with a separate temperature and density. These two states are kept in pressure equilibrium, and correspond roughly to the cold swept-up ISM and the hot SN-heated interior. Mass flows from the cold phase to the hot via thermal evaporation (Cowie & McKee 1977) until the entire cold phase has been evaporated. This evaporation process can continue by stochastically evaporating cool neighbors of hot, SN-heated gas particles. Within resolved hot bubbles, temperatures gradients are smoothed by ther-

mal conduction. The superbubble model is better able to capture the effects of multiple SNe occurring over a range of timescales, drives stronger outflows, and produces a more realistic gas phase diagram than the earlier blastwave model. For superbubble feedback, energy is deposited at a rate of $1 \times 10^{51} \text{ erg per SN}$. Azartash-Namin et al. (2024) ran one set of the Marvel simulations with both feedback models, and demonstrated that they produce very similar dwarf galaxies – reproducing their expected stellar mass, size, metallicity, and bursty star formation.

Halos are identified with AMIGA’s HALO FINDER (AHF) (Gill et al. 2004; Knollmann & Knebe 2009). We define the virial radius of a halo as the distance from the center of mass in which the average halo density is 200 times that of the critical density at a given redshift. Much of the analysis is performed using PYNBODY¹ (Pontzen et al. 2013), a python package for SPH + N-body simulations.

CHANGA calculates the $H I$ mass fraction for every gas particle throughout the simulation. The gas fraction is based on the particle’s temperature and density, heating from the cosmic UV background radiation and young stars, H_2 self-shielding, and dust shielding in $H I$ and H_2 . We can use the $H I$ gas fractions and sum over particles to get the total $H I$ mass. Similarly, the total stellar mass and halo mass are calculated by summing over particles within the virial radius (R_{200}). Munshi et al. (2013) estimated that photometric observational methods yield stellar masses that are $\sim 60\%$ of simulation values, so we include this factor for a more direct comparison to observations. Throughout this study, any stellar mass will be 60% of the simulation total. The total halo mass (M_{200}) uses the same virial constraint as AHF at $200\rho_c(z)$.

2.1 Sample Selection

The faintest galaxies in most bTFR studies have stellar masses on the order of $10^7 M_\odot$ (e.g., Bradford et al. 2015; Lelli et al. 2016a). In the case of McQuinn et al. (2022), a few galaxies have stellar masses $\sim 4 \times 10^6 M_\odot$. To better understand the bTFR turndown, our sample includes dwarf galaxies with $M_\star > 10^6 M_\odot$. We also require that each galaxy has $M_{HI} > 10^6 M_\odot$ in order to have enough gas for observable rotation speeds. We select isolated, central galaxies to focus on the connection between gas and dark matter kinematics without significant complications from galaxy-galaxy interactions. Bradford et al. (2016) required that any galaxy in their bTFR sample with $M_\star < 10^{9.5} M_\odot$ be isolated, with the 2D projected distance to the nearest most massive host $< 7 \text{ Mpc}$. All of our simulated galaxies have $M_\star < 10^{9.5} M_\odot$, and we consider one to be ‘isolated’ if there are no galaxies more massive than the host within its virial radius. Our sample includes 66 dwarf galaxies, in which 39 are from the Massive Dwarfs suite and 27 are from the Marvel suite. Our galaxy mass ranges are $\log(M_\star [M_\odot]) = 6.03 - 9.25$, $\log(M_{\text{bary}} [M_\odot]) = 6.77 - 9.83$, and $\log(M_{200} [M_\odot]) = 9.58 - 11.2$. We define the total baryonic mass as $M_{\text{bary}} = M_\star + 1.4 M_{HI}$, where the factor of 1.4 accounts for helium (e.g., Arnett 1996; Bradford et al. 2016) and metals in the gas phase. Our galaxy sample consists of 4 stellar-dominated galaxies and 62 gas-dominated galaxies, as shown in Figure 1. Based on classification using the moment of inertia tensor, we find that 34 out of 66 of our galaxies have distinct gaseous disks, while the remaining galaxies – mostly with $M_\star < 10^8 M_\odot$ – are more irregular (Keith et al. 2025).

¹ <https://pynbody.github.io/pynbody/>

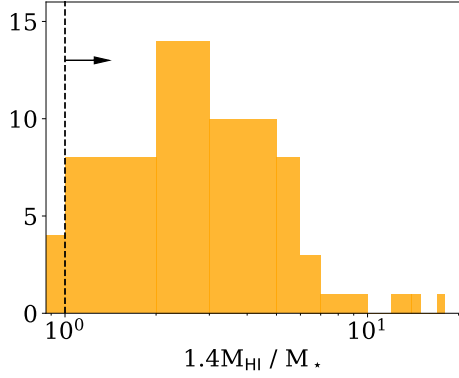


Figure 1. Histogram of gas to stellar mass ratios for our galaxy sample, which range from 0.54 to 18.2. We use $M_{\text{gas}} = 1.4 M_{\text{HI}}$. Galaxies to the right of the black dashed vertical line are gas-dominated, which is most of our sample.

2.2 Spatially unresolved H I profiles

We use the program TIPSy² (Katz & Quinn 1994) to create mock H I data cubes from our simulations. We use these data cubes to derive spatially unresolved velocity widths (W_{10} , W_{20} , and W_{50} , as defined in the next section). With TIPSy, we can visualize star, gas, and dark matter particles, and orient the halo at different inclinations. To make a data cube, we center on the halo of interest, subtract its center of mass velocity so that the profile is centered at 0 km s⁻¹, and orient it edge-on ($i = 90^\circ$) or at a random inclination. The disk is aligned based on the angular momentum of gas particles in a central region of high-density gas that is visually identified. The angular momenta for stars and dark matter are ignored. We orient the angular momentum vector around the z -axis of the simulation and align the galaxy according to this.

After we give TIPSy a viewing angle, the code considers the line-of-sight velocity for each particle. Our simulations track the velocity of each particle according to Newton’s equations of motion, and we have to separately consider velocity contributions from turbulence or thermal broadening. Dwarf galaxies can have velocity dispersions on the order of their rotation velocities, $\sim 10\text{--}15$ km s⁻¹ (e.g., Tamburro et al. 2009), and dispersions are likely driven by thermal velocities or SNe (Tamburro et al. 2009; Stilp et al. 2013b,a). Our simulations have SNe injecting thermal energy into the interstellar medium. To account for thermal broadening in the H I profiles, TIPSy ‘smears’ the velocity contribution from each gas particle into a Gaussian centered on the line-of-sight velocity with a standard deviation of $\sigma = \sqrt{kT/(\mu m_p)}$, where T is the gas particle’s temperature, m_p is the proton mass, and μ is the mean molecular weight of the ISM. The mean molecular weight determines what the average particle mass is as a fraction of a proton mass, and this is calculated based on the metallicity and ionization state of the gas.

We use a fixed velocity resolution of 2.6 km s⁻¹ and measure each galaxy over the velocity range -200 to 200 km s⁻¹. This velocity resolution is set to match the quality of Green Bank Telescope observations in Bradford et al. (2015). Our data cubes have fixed spatial axes spanning from -100 to 100 kpc across each galaxy with a resolution of 3.7 kpc, though the spatial resolution has little impact on the unresolved linewidth results. In this work, we do not consider beam smearing effects or observational noise.

2.3 Inclinations

Inclination corrections to observed velocities can be substantial at the dwarf galaxy scale. As previously described, we orient both our disk and irregular galaxies such that the total angular momentum vector of the central gas lies along the z direction, and then measure our H I linewidths edge-on. Of course, this is not the same method employed in observations, where the projected elliptical shape of the galaxy is measured to determine an inclination. Usually, inclination angles are calculated based on the major and minor axes of the galaxy’s stellar components from optical observations. Galaxies with inclinations lower than $i \lesssim 30^\circ - 40^\circ$ are often not included in samples, since projection uncertainties are significant (e.g., Oman et al. 2016; Read et al. 2016; Lelli et al. 2016b; Read et al. 2017; McQuinn et al. 2022). Observations typically report inclination-corrected rotation velocities, and so we use the edge-on velocities regardless of galaxy morphology.

At $M_\star \lesssim 10^8 M_\odot$, our simulated dwarfs are predominantly irregular rather than disk (Keith et al. 2025). For these lowest-mass dwarf galaxies, we have found that our orientation method does not always yield a result that is edge-on by visual inspection. It is possible that there is no orientation that yields an apparent edge-on result, given their irregular nature. Although the inclinations for these irregular galaxies are difficult to measure and correct for, the Gaussian H I profiles of these lower-mass dwarf galaxies do not vary much by viewing angle (as quantified in the errors presented in Section 3.2). Our inclination procedure with simulations allows us to include dwarf galaxies that would otherwise be removed from observational samples.

Despite the differences in methodology from observations, we keep our full dwarf sample in order to quantify trends to as low mass as possible. However, we highlight that systematic differences between our H I linewidth results versus observations likely come from these unknown inclinations *and* the inclusion of more irregular, low-mass galaxies. Throughout this work, we only show inclination-corrected linewidths (by using the edge-on results) and compare to inclination-corrected values from observations.

2.4 Definitions for Velocities and Radii

There are a number of different ways to measure rotation velocity, and at different radii. In this work, we aim to understand how the different methods impact the determined bTFR. The methods for velocities and corresponding radii in this work are:

- $V_{\text{max,circ}}$ and $R_{\text{max,circ}}$: the maximum rotation velocity calculated based on concentric shells of the enclosed mass, as in the ‘dynamical mass’, where the circular rotation velocity is defined as $V(R) = \sqrt{GM(<R)/R}$. The radius corresponding to $V_{\text{max,circ}}$ is $R_{\text{max,circ}}$. The PYNBODY profile class can calculate a rotation curve based on the mass enclosed. This is an idealized measurement enabled by the use of simulations. For our dwarf galaxies, $R_{\text{max,circ}}$ is often beyond the radius at which H I could be observationally detected.

- $V_{\text{max,mid}}$ and $R_{\text{max,mid}}$: the maximum rotation velocity calculated based on the midplane gravitational potential. $R_{\text{max,mid}}$ is the radius at which $V_{\text{max,mid}}$ occurs. The midplane rotation velocity follows the relation $V(R) = \sqrt{R \frac{\delta\Phi}{\delta R}}$, where the calculated velocity is based on the radial component of the gravitational acceleration of the entire galaxy using a few sample points in the midplane. PYNBODY aligns the galaxy and determines this midplane according to the angular momenta of gas particles within 10 kpc from the halo’s

² <https://github.com/N-BodyShop/tipsy>

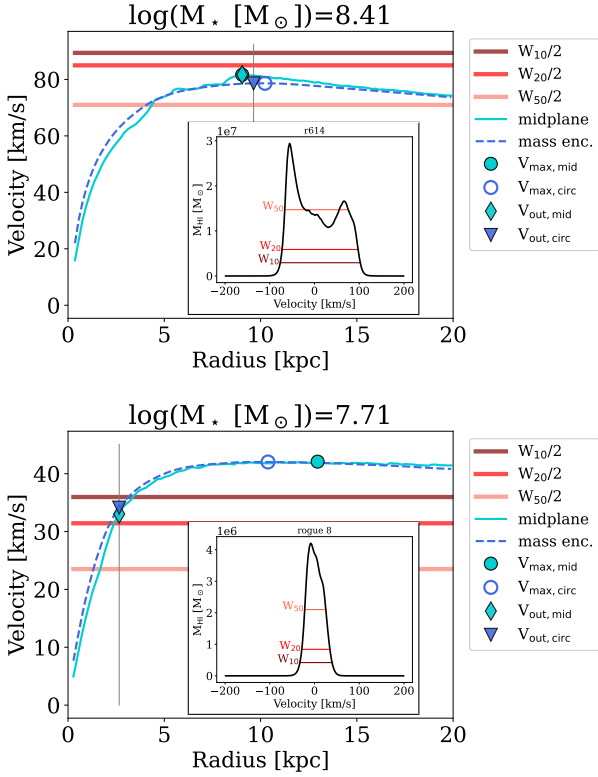


Figure 2. Top panel shows the H I profile (inset) and rotation curve for r614 from the Massive Dwarfs suite, which is disk and has a higher stellar mass. Bottom panel is similar but for Rogue 8 from the Marvel suite, which is irregular and lower in mass. For the rotation curves, the solid cyan line is calculated using the midplane potential, whereas the dashed blue line uses the mass enclosed. The open blue point is $V_{\text{max,circ}}$, the solid cyan point is $V_{\text{max,mid}}$, the blue triangle represents $V_{\text{out,circ}}$, and the cyan diamond represents $V_{\text{out,mid}}$. The vertical grey line denotes the radius R_1 , where the H I surface density drops below $1 \text{ M}_\odot \text{ pc}^{-2}$. H I linewidths (W_x) are measured from the inset H I profiles. Each linewidth is represented by a horizontal line of a different color ($W_{10}/2$ is maroon, $W_{20}/2$ is red, and $W_{50}/2$ is salmon). r614 has a higher stellar mass and exhibits the double-horned profile, while Rogue 8 has a more Gaussian profile.

center. We orient the galaxy with the total gas angular momentum vector aligned with the z -axis, so that the disk is in the $x - y$ plane. Then, we calculate the rotation speed from this method as a function of radius with `PYNBODY`'s profile class. Most of our galaxies are disk and align well in the $x - y$ plane. However, we use this same methodology for all of the galaxies, even the non-disk ones where a disk plane is not well-defined, in order to calculate the midplane potential.

- **$V_{\text{out,circ}}$ and $R_{\text{out,circ}}$:** R_1 is the 2D projected size of the H I disk where its surface density drops below $1 \text{ M}_\odot \text{ pc}^{-2}$ (corresponding to a column density of $N_{\text{HI}} \sim 1.25 \times 10^{20} \text{ cm}^{-2}$). We set this value to match the canonical main H I disk limit in other works (e.g., Broeils & Rhee 1997; Wang et al. 2016). $V_{\text{out,circ}}$ is the maximum rotation speed using the mass-enclosed method at $R \leq R_1$, and $R_{\text{out,circ}}$ is the corresponding radius.

- **$V_{\text{out,mid}}$ and $R_{\text{out,mid}}$:** uses the same R_1 value, though the corresponding velocity and radius are determined from the rotation curve using the midplane gravitational potential.

- **W_x and R_x :** W_{10} , W_{20} , and W_{50} are the H I profile's width at different percentages of the peak flux height; 10%, 20%, and 50%,

respectively. The corresponding radius, $R_{x,\text{circ}}$, is where the line width $W_x/2$ intersects the circular rotation curve. For some cases, $W_x/2$ may not exactly intersect the rotation curve (see Figure 2, top panel as an example). To obtain the equivalent radius, we calculate the difference between the rotation curve and $W_x/2$, and define $R_{x,\text{circ}}$ as the corresponding radius with the smallest difference within 5 km s^{-1} of $W_x/2$.

The H I linewidths (W_{10} , W_{20} , and W_{50}) are spatially unresolved, while all other velocities are from rotation curves that are resolved as a function of radius. For the spatially resolved methods, we use linearly-spaced bins, starting at a radius of $3R_{\text{soft}}$ and extending out to 20 kpc with 100 bins. The number of radial bins was selected based on the criteria from Power et al. (2003), where ≥ 3000 particles per enclosed region are needed for accurate circular velocities in dense central regions. R_{soft} is the gravitational force softening length for each simulation suite: 0.087 kpc for the Massive Dwarfs and 0.060 kpc for Marvel. The spacing between radial bins is ~ 0.2 kpc. Figure 2 demonstrates how these velocities and radii compare for a higher-mass galaxy (r614) and lower-mass galaxy (Rogue 8) in our sample. r614 demonstrates how a higher-mass galaxy exhibits a flat rotation curve at the fiducial observational limit of $1 \text{ M}_\odot \text{ pc}^{-2}$, as well as a classic double-horned H I profile. For a lower-mass galaxy like Rogue 8, the H I gas does not extend as far out radially. Therefore, the galaxy's H I velocities (spatially resolved or unresolved) do not match the galaxy's actual $V_{\text{max,mid}}$ or $V_{\text{max,circ}}$.

3 RESULTS

3.1 Comparing Stellar and H I Properties to Observations

Before analyzing the bTFR in our simulated dwarf galaxies, it is crucial to check whether we have achieved realistic baryonic properties for each galaxy. First, we check masses. Figure 3 shows the SMHM relation for our sample in the left panel. We compare the SMHM relation from our simulations to the abundance matching results from Behroozi et al. (2013) and Moster et al. (2013). For $M_{200} \gtrsim 3 \times 10^{10} \text{ M}_\odot$, our SMHM relation matches Moster et al. (2013), whereas at $M_{200} \lesssim 3 \times 10^{10} \text{ M}_\odot$, our data lie within the range of Behroozi et al. (2013) and Moster et al. (2013). In the right panel of Figure 3, we show the baryon-halo mass relation for our sample. We define the total baryonic mass as $M_{\text{bary}} = M_\star + 1.4M_{\text{HI}}$, where the 1.4 factor also accounts for helium and metals in the gas phase. We also compare our baryonic content to the cosmic fraction $f_b = \Omega_b/\Omega_m = 0.1582$ using the Planck Collaboration et al. (2020) values: $\Omega_m = 0.315$, $\Omega_b h^2 = 0.0224$, and $h = 0.674$. Our baryon fractions range from $\sim 0.01 f_b - 0.5 f_b$, and decrease with lower halo masses. Below $M_{200} \lesssim 3 \times 10^{10} \text{ M}_\odot$, we find more scatter in our SMHM relation and baryon-halo mass relation (see also Munshi et al. 2021).

To assess whether our H I mass content is realistic, we plot M_{HI} as a function of M_\star in the top panel of Figure 4. We compare our simulated galaxies to the observed galaxies in Bradford et al. (2015) and McQuinn et al. (2022). Bradford et al. (2015) combined data from their own observations, the ALFALFA survey (Haynes et al. 2011), and Geha et al. (2006). In this comparison, we omit the ALFALFA data since Haynes et al. (2011) selected galaxies by H I mass rather than stellar mass, which has been shown to be biased toward higher H I masses than a stellar-mass selected sample (Catinella et al. 2010).

After confirming that our masses are consistent with observations, we check the H I size-mass relationship in the bottom panel of Figure 4. The size is defined as the diameter where the H I surface density

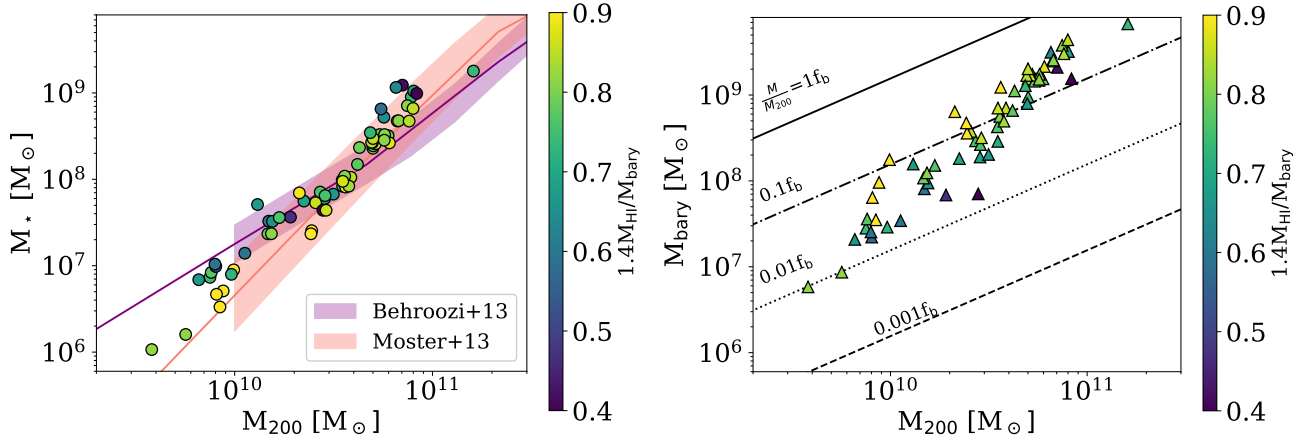


Figure 3. Left panel shows the SMHM relation (circle markers), while the right panel shows the baryon-halo mass relation (triangle markers). Each marker is colored by the gas fraction $1.4M_{\text{HI}}/M_{\text{bary}}$ and shows the gas-rich nature of our sample where most of the galaxies have gas fractions > 0.7 . We compare our SMHM relation to abundance matching results from Behroozi et al. (2013) (purple shaded region) and Moster et al. (2013) (red shaded region) with $1-\sigma$ error. Both abundance matching results were determined down to $M_{200} \sim 10^{10} M_{\odot}$, and we extrapolate the relations below this halo mass, indicated by the end of the shaded regions. Our stellar masses are 60% of the total stellar mass calculated from the simulations, as this is a better match to photometrically-derived observational methods (Munshi et al. 2013). Our simulated galaxies are consistent with the SMHM constraints from abundance matching. We compare baryon mass fractions to the cosmic value ($f_b = \Omega_b/\Omega_m = 0.1556$) using cosmological values from Planck Collaboration et al. (2020)). We plot $M/M_{200} = 1f_b$ (solid line), $M/M_{200} = 0.1f_b$ (dotted dashed line), $M/M_{200} = 0.01f_b$ (short dashed line), and $M/M_{200} = 0.001f_b$ (long dashed line). Both the SMHM and baryon-halo mass relations exhibit more scatter at $M_{200} < 3 \times 10^{10} M_{\odot}$.

has dropped to $1 M_{\odot} \text{pc}^{-2}$, similar to observations. We compare the H I size-mass relation from the simulated dwarf galaxies to the observations from Wang et al. (2016), which follows the trend from Broeils & Rhee (1997) (B97), and has been confirmed by recent WALLABY (Deg et al. 2024) and FEASTS results (Wang et al. 2025). Our galaxies fit in the $3-\sigma$ scatter of Wang et al. (2016), represented by the grey line and shaded region. Stevens et al. (2019) found that the H I size-mass relation is robust to gas stripping and galaxy population (centrals versus satellites), so matching this relation mostly confirms that our feedback is of appropriate strength and does not disrupt the H I disk.

Finally, because it has been suggested that galaxies simply evolve along the H I size-mass relation (Stevens et al. 2019), we check whether our H I disks extend to realistic radii by instead comparing them against stellar properties. In the top panel of Figure 5, we compare our H I sizes against the absolute B -band magnitude (M_B). We compare the trend in our simulations to the observations in Wang et al. (2016). We determine the galaxy’s B -band brightness profile out to the virial radius with PYNBODY’s profile class, which uses the Marigo et al. (2008) and Girardi et al. (2010) stellar population models. Then, we calculate the total B -band luminosity (L) by summing over radial bins, and turn this value into a magnitude with the relation $M_B = -2.5 \log_{10}(L * \alpha)$, where the conversion factor is $\alpha = 2.35 \times 10^9 \text{ pc}^2 \text{ arcsec}^{-2} \text{ erg}^{-1} \text{ s}$. Our galaxy sizes are within the observed range for $M_B = -12.5$ to -18.0 , though we may not have examples of the most extended H I disks. This may be due to differences in our sample sizes and selection functions, since H I surveys are more sensitive to galaxies with more H I flux.

If our galaxies have H I disks that are realistic in size, then their H I linewidths should also match the observational range. In the bottom panel of Figure 5, we assess how well W_{20} matches between simulations and observations at a given M_* . Bradford et al. (2015) corrected for inclination (i) and redshift (z) broadening in their linewidths, reporting the value $V_{20,i} = W_{20}/[2 \sin i(1+z)]$ as a maximum rotation velocity. Our edge-on linewidths should be comparable to the

inclination-corrected velocities in Bradford et al. (2015), and so we plot their $2V_{20,i}$ against our W_{20} . Our linewidths are indeed consistent with the range from Bradford et al. (2015), suggesting that our baryonic feedback is realistic, and so is the thermal broadening we used to make mock data cubes.

3.2 bTFR with Different Velocity and Rotation Curve Definitions

Having shown that our simulations follow a number of observed scaling relations related to H I, we now analyze the bTFR according to different velocity methods.

bTFR using the maximum halo speed: Modeling the halo’s circular velocity based on the total mass enclosed in spherical shells is common in bTFR observations (e.g., Trujillo-Gomez et al. 2018; McQuinn et al. 2022; Lelli et al. 2019), so we use this definition as our reference point. In Figure 6, we show that the circular velocity of the halo ($V_{\text{max,circ}}$, black points) exhibits a turndown in the bTFR at $M_{\text{bary}} \lesssim 10^{8.5} M_{\odot}$, corresponding to velocities $\lesssim 50 \text{ km s}^{-1}$, as galaxy formation becomes inefficient. Our bTFR trend is consistent with the turndown predicted by Sales et al. (2017) for the halo circular speed in the APOSTLE simulations (orange solid line).

We can also calculate the halo’s rotation speed using the midplane gravitational potential ($V_{\text{max,mid}}$, black points – top right panel in Figure 6) instead of the enclosed mass. If galaxies are in dynamic equilibrium and the assumption of spherical symmetry is valid, the two methods should return the same velocity. However, as explored in a number of previous works (e.g., Read et al. 2016; El-Badry et al. 2017; Verbeke et al. 2017; Downing & Oman 2023; Sands et al. 2024), dwarf galaxies have bursty star formation histories with feedback that frequently drives them out of dynamical equilibrium. This effect is likely to become more pronounced as galaxy mass decreases and the gravitational potential well becomes shallower and more susceptible to feedback. Additionally, velocity dispersion becomes more dominant as galaxy mass decreases and rotation velocity

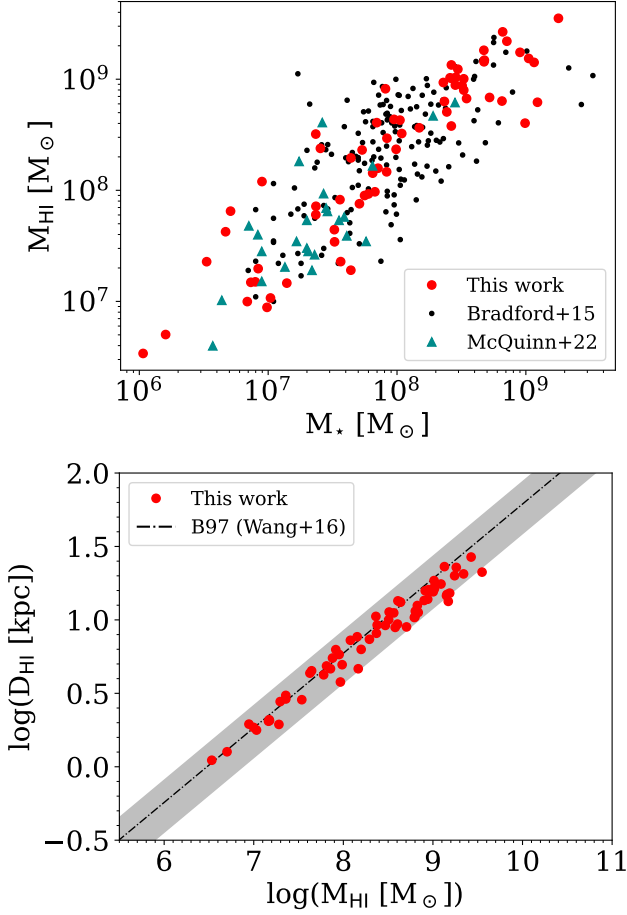


Figure 4. The top panel compares the total H I mass as a function of stellar mass in our simulations (red points) to observations from [Bradford et al. \(2015\)](#) (black points) and [McQuinn et al. \(2022\)](#) (cyan triangles). The bottom panel compares our simulations (red points) to the empirical relationship (dotted-dashed line) between the size and total mass of H I gas in galaxies ([Broeils & Rhee 1997](#)). In this study and the observations compared here, the H I size is defined as the radius where the H I surface density has dropped to $1 \text{ M}_\odot \text{ pc}^{-2}$. The grey shaded region shows the $3\text{-}\sigma$ scatter in the observations from [Wang et al. \(2016\)](#).

declines, such that circular velocity is no longer an accurate measure of velocity. Because of these effects, using the midplane gravitational potential may be a more accurate tracer of the underlying mass distribution, and perhaps more comparable to what an observer might measure at lower rotation speeds. However, for our sample the overall differences in the two methods are subtle (as seen in Figure 2). Differences between the mass enclosed and midplane methods tend to be more significant at smaller radii, but our measurements for the maximum halo speed are measured at larger radii and hence both methods produce similar results for the bTFR. When using $V_{\text{max,mid}}$, we again find a turndown at $M_{\text{bary}} \lesssim 10^{8.5} \text{ M}_\odot$.

bTFR using spatially resolved methods: At an H I surface density of $1 \text{ M}_\odot \text{ pc}^{-2}$, we measure the 2D projected radius, R_1 . Then, we find the maximum rotation speeds for each rotation curve method at radii within R_1 , which we call $V_{\text{out,circ}}$ (which uses the enclosed mass) and $V_{\text{out,mid}}$ (which uses the midplane potential). The top left panel of Figure 6 shows the bTFR when we use $V_{\text{out,circ}}$ (blue triangle markers), while the top right panel shows the bTFR when using $V_{\text{out,mid}}$ (cyan diamond markers). We compare our spatially resolved

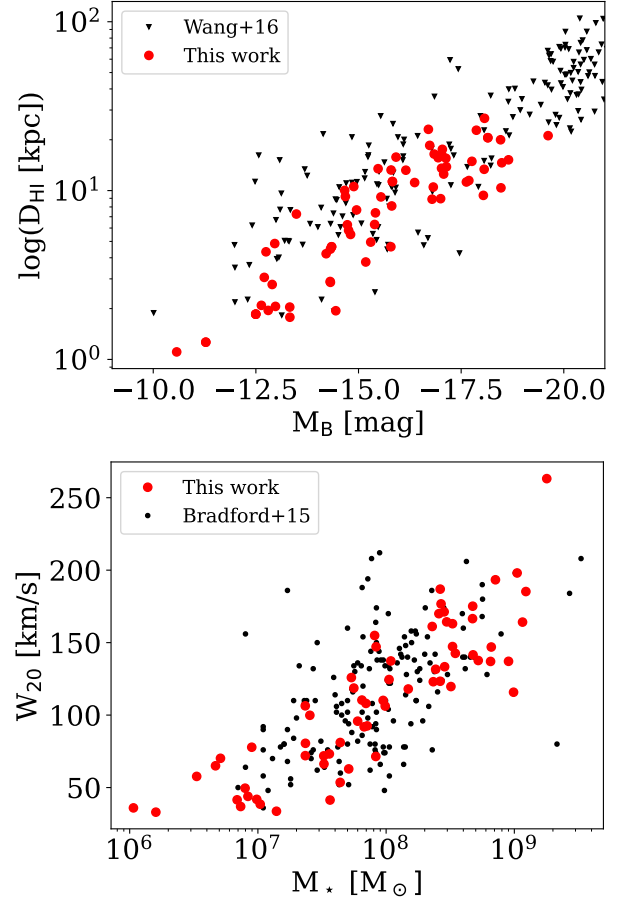


Figure 5. The top panel compares the H I size to the stellar content as quantified by the absolute B -band magnitude. We calculate the cumulative B -band magnitude (red points) and compare our data to observations from [Wang et al. \(2016\)](#) (black triangles). In general, we find the H I properties of our simulated dwarf galaxies to be comparable to observed dwarf galaxies, though we may lack the most extended H I disks. The bottom panel compares our linewidths from mock H I data cubes (red points) to that of observed linewidths (black points) from [Bradford et al. \(2015\)](#) for a given stellar mass. The observed linewidths are corrected for inclination and redshift broadening, and we plotted their values for $2V_{20,i}$ to compare with our edge-on values of W_{20} , i.e., both the simulated and observed samples are inclination-corrected.

results to the V_{max} trend in [Lelli et al. \(2019\)](#) (grey dashed line), which uses the maximum velocity from observed rotation curves, for galaxies that have both flat and rising rotation curves. From their Table 1, [Lelli et al. \(2019\)](#) measured a slope = 3.52, intercept = 2.59, and vertical scatter = 0.27 (grey shaded region) with a sample of 153 galaxies. Both spatially resolved H I methods are consistent with observations as they each follow a power-law trend and do not exhibit a turndown. We show representative error bars on the lowest-mass galaxy, in which we estimate the observational errors for velocity and mass (discussed further in Section 3.4).

bTFR with H I Linewidths: In the bottom panel of Figure 6, we show the bTFR when using spatially unresolved H I linewidths. We compare the linewidths (square markers; W_{10} in maroon, W_{20} in red, and W_{50} in salmon) to $V_{\text{max,circ}}$ (black markers). The observational sample compared here is different than in the other two panels. The dashed line shows the bTFR result from [Bradford et al. \(2016\)](#), which uses the W_{20} linewidths for 930 isolated galaxies and has a slope = 3.24, intercept = 3.21, and vertical scatter = 0.25 (grey

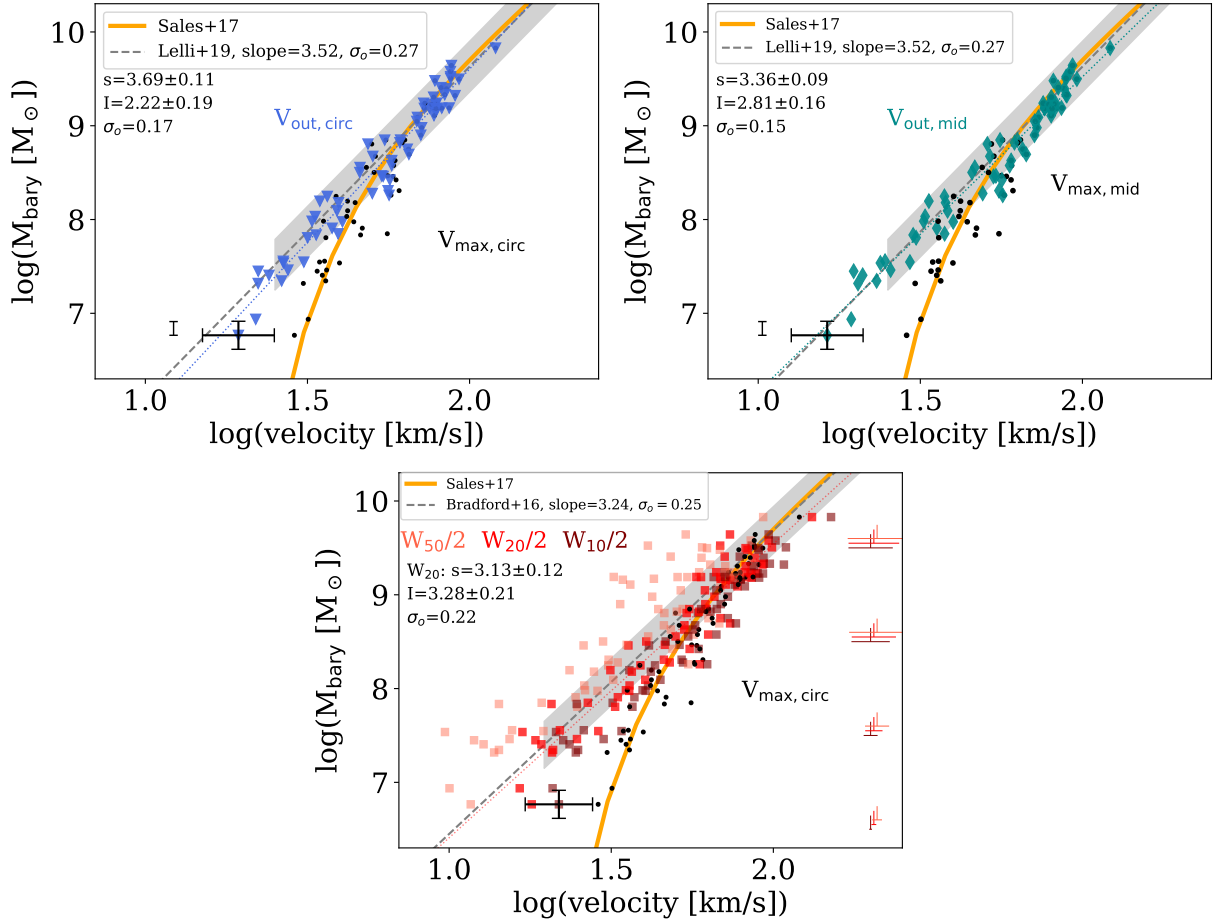


Figure 6. The bTFR from our simulations (markers), compared to constraints from observations in Lelli et al. (2019) (grey dashed line in the top panels) and Bradford et al. (2016) (grey dashed line in the bottom panel), as well as the APOSTLE simulations (Sales et al. 2017) (orange line). Upper left panel shows the bTFR when using $V_{\text{out,circ}}$ (spatially resolved mass-enclosed), upper right panel shows the bTFR with $V_{\text{out,mid}}$ (spatially resolved midplane potential), and the bottom panel shows the bTFR with H I linewidths ($W_{50}/2$ in salmon, $W_{20}/2$ in red, $W_{10}/2$ in maroon). Halo speeds are plotted as $V_{\text{max,circ}}$ (mass-enclosed, black points) and $V_{\text{max,mid}}$ (midplane, black points, top-right). Estimated observational errors are plotted on the lowest mass galaxy in each panel, and are derived in Section 3.4. In the top panels, the mass error to the left of the observational errors shows the variance in stellar mass from simulations to observations according to Munshi et al. (2013). In the bottom panel, simulation variance in stellar mass and linewidths (due to inclination angle) is plotted in the colored error bars. We find a bTFR turndown using the halo’s maximum rotation speed (black markers), for either the mass-enclosed or gravitational midplane potential methods. However, H I gas does not trace the halo’s maximum rotation speed at rotation speeds $< 50 \text{ km s}^{-1}$ (or $M_{\text{bary}} \lesssim 10^{8.5} M_{\odot}$).

shaded region). As established by other works (Macciò et al. 2016; Brooks et al. 2017; Dutton et al. 2019; Sardone et al. 2024), W_{50} often underestimates the halo rotation speed ($V_{\text{max,circ}}$). W_{20} and W_{10} trace the halo at higher masses, but do not exhibit the bTFR turndown at lower masses. All of our linewidths are from the H I profile when viewing the galaxy edge-on ($i = 90^\circ$), and therefore are inclination-corrected.

Errors on the lowest-mass galaxy are based on percent errors in single-dish data, and this is discussed further in Section 3.4. We plot the variance in our simulations on the right side of the plot for W_{10} (maroon), W_{20} (red), and W_{50} (salmon) for each mass bin spanning 1 order of magnitude. H I linewidths vary depending on the viewing angle and mass of the galaxy. We calculate the difference between the linewidth when the galaxy is viewed edge-on versus at a random inclination angle, and then average over all of the galaxies in a given mass bin. Despite the uncertainty on inclination angle for the lower-mass, irregular galaxies, the variance error bars are smallest in this regime as the Gaussian H I profiles do not vary much with viewing

angle. In this regime, the variance is small compared to the estimated observational errors.

In summary, a turndown in the bTFR is predicted no matter the method used to find the *halo*’s maximum rotation speed, either the mass-enclosed (black points, top left panel) or gravitational midplane potential (black points, top right panel). However, the maximum halo value is not generally recoverable with H I, whether for spatially resolved methods at the limit $\Sigma_{\text{out}} = 1 M_{\odot} \text{ pc}^{-2}$, or the unresolved H I linewidths. For resolved rotation curves, using the enclosed mass to estimate the speed results in only slightly higher rotation speeds for lower-mass galaxies as compared to using the midplane potential (at most, $\sim 15\%$ difference), but neither shows a turndown when measuring the maximum resolved H I velocity. For the unresolved H I profiles, no measurement is able to recover the underlying turndown in the bTFR. These results have major implications for observational studies. We further investigate the physical origins of these results, and their implications, below.

Velocity (V)	Slope (s)	Intercept (I)	σ_o
$V_{\text{out,circ}}$	3.69 ± 0.11	2.22 ± 0.19	0.17
$V_{\text{out,mid}}$	3.36 ± 0.09	2.81 ± 0.16	0.15
W_{10}	3.40 ± 0.12	2.66 ± 0.21	0.20
W_{20}	3.13 ± 0.12	3.28 ± 0.21	0.22
W_{50}	2.59 ± 0.16	4.52 ± 0.25	0.33

Table 1. The linear regression fit parameters and errors for each H I velocity method.

3.3 bTFR Slopes and Fit Parameters

For each velocity method, Table 1 shows fits to the equation

$$\log(M_{\text{bary}}[M_{\odot}]) = s \log(V[\text{km s}^{-1}]) + I, \quad (2)$$

where s and I are free parameters. The fitted parameters and errors are determined from `numpy.polyfit`. For our vertical scatter, or ordinary least squares error (σ_o), we use the definition from Lelli et al. (2019) which sums over N galaxies (index j):

$$\sigma_o = \text{OLS error} = \sqrt{\frac{1}{N} \sum_j [\log(M_{\text{bary},j}) - s \log(V_j) - I]^2}. \quad (3)$$

For the spatially resolved velocity methods, our bTFR slope using $V_{\text{out,circ}}$ (3.69 ± 0.11) is consistent with studies in a similar baryonic mass range. Lelli et al. (2019) found a bTFR slope of 3.52 ± 0.07 , and Šiljeg et al. (2024) found that classical dwarfs observed with Apertif follow this relation. Deg et al. (2024) used early WALLABY observations and found a slope of 3.3 ± 0.2 . Our value is less steep than the slope from Stark et al. (2009) (3.94 ± 0.07 (random) ± 0.08 (systematic)), and this is likely due to their sample having fewer low-mass galaxies ($M_{\text{bary}} < 10^8 M_{\odot}$). Stark et al. (2009) also select for gas-rich galaxies that reach a flat rotation curve, which has been shown to produce a slope closer to 4 (Bradford et al. 2016).

For the spatially unresolved methods, our bTFR slope for W_{50} (2.59 ± 0.16) is shallower, while the slopes for W_{20} (3.13 ± 0.12) and W_{10} (3.40 ± 0.12) are closer to observations. Using W_{20} , Bradford et al. (2016) measured a slope of 3.24 ± 0.05 , and Lelli et al. (2019) measured 3.75 ± 0.08 . We expect W_{10} and W_{20} to have steeper bTFR slopes than W_{50} , since $W_{50} < W_{20} < W_{10}$ based on the shape of H I profiles. This is consistent with previous studies (Bradford et al. 2016; El-Badry et al. 2017; Lelli et al. 2019; Sardone et al. 2024). Our bTFR slopes from H I linewidths may not exactly match observations due to differences in how we treat inclination angle (as discussed in Section 2.3) and the inclusion of more irregular, lower-mass galaxies in our sample.

We also determine best-fit relationships between the H I velocities and the maximum rotation speeds, $V_{\text{max,mid}}$ and $V_{\text{max,circ}}$. For $V_{\text{max,circ}}$, which uses the mass-enclosed gravitational potential, the equations relating the maximum halo speed to the H I velocities are:

$$\begin{aligned} V_{\text{out,circ}} &= (1.15 \pm 0.02)V_{\text{max,circ}} + (-12.38 \pm 1.18) \\ V_{\text{out,mid}} &= (1.23 \pm 0.03)V_{\text{max,circ}} + (-16.62 \pm 1.64) \\ W_{10}/2 &= (1.28 \pm 0.05)V_{\text{max,circ}} + (-16.62 \pm 3.54) \\ W_{20}/2 &= (1.17 \pm 0.06)V_{\text{max,circ}} + (-15.87 \pm 3.83) \\ W_{50}/2 &= (0.87 \pm 0.08)V_{\text{max,circ}} + (-10.3 \pm 5.20). \end{aligned}$$

The equations relating $V_{\text{max,mid}}$ (assuming the midplane gravita-

tional potential) to the H I velocities are:

$$\begin{aligned} V_{\text{out,circ}} &= (1.10 \pm 0.02)V_{\text{max,mid}} + (-10.84 \pm 1.18) \\ V_{\text{out,mid}} &= (1.18 \pm 0.02)V_{\text{max,mid}} + (-15.17 \pm 1.40) \\ W_{10} &= (1.23 \pm 0.05)V_{\text{max,mid}} + (-15.22 \pm 3.33) \\ W_{20} &= (1.13 \pm 0.05)V_{\text{max,mid}} + (-14.77 \pm 3.59) \\ W_{50} &= (0.85 \pm 0.07)V_{\text{max,mid}} + (-10.15 \pm 4.90). \end{aligned}$$

Finally, we determine the relation between the maximum halo speeds $V_{\text{max,mid}}$ and $V_{\text{max,circ}}$:

$$V_{\text{max,mid}} = (1.04 \pm 0.01)V_{\text{max,circ}} + (-1.34 \pm 0.47).$$

3.4 Estimate of Observational Errors

The bTFR compares a galaxy's baryonic mass ($M_{\text{bary}} = M_{\star} + 1.4M_{\text{HI}}$) and rotation velocity, and in this section we elaborate on our errors for each axis. We do not perform mock observations for our simulated dwarf galaxies. However, we attempt to plot our bTFR trends with reasonable errors to determine the significance of differences between H I and halo velocities.

Our baryonic mass error must account for errors in stellar mass and H I mass. For stellar mass, we use an uncertainty of 0.12 dex (33%) adopted by McQuinn et al. (2022). This uncertainty considers the variance in mass-to-light ratios ranging from 0.45–0.6 at $3.6 \mu\text{m}$, which is the upper-end of uncertainties from calibrations like Zhu et al. (2010), McGaugh & Schombert (2014), and Meidt et al. (2014), resulting in a fractional uncertainty of $(0.6 - 0.45)/0.45 = 0.33$. For H I mass errors, we adopt the error function from Haynes et al. (2018), which propagates distance (D) and flux (S_{21}) percent uncertainties:

$$\sigma_{\log(M_{\text{HI}})} = \frac{\sqrt{\left(\frac{\sigma_{S_{21}}}{S_{21}}\right)^2 + \left(\frac{2\sigma_D}{D}\right)^2} + 0.12}{\ln 10}. \quad (4)$$

We use a signal-to-noise ratio of 6.5 (15% error), and this is the threshold used by Haynes et al. (2018). We adopt a distance uncertainty of $\sim 3\%$, which is the average for the sample in McQuinn et al. (2022). Distance uncertainties in this range require primary distance methods such as the tip of the red giant branch. Based on this distance uncertainty, we find an H I mass uncertainty of 0.08 dex (21%). Finally, we take the log-space stellar and H I mass errors in quadrature to get 0.15 dex (41%) as the baryonic mass error.

For the total error in velocity, we consider the uncertainty from turbulent motion (dispersion) and the uncertainty in measuring the rotation speed. The asymmetric drift correction from gas turbulence is usually approximated with a value of $\sigma_{\text{asd}} = 8 \pm 2 \text{ km s}^{-1}$ (Stilp et al. 2013b). By taking the logarithm of the upper limit as a fraction of the fiducial value, we get $\log(1.25\sigma_{\text{asd}}/\sigma_{\text{asd}}) = 0.1 \text{ dex}$ (25% error) as the dispersion uncertainty. For the uncertainty of spatially resolved velocities, we use 0.05 dex (13%), which is the average for galaxies from McQuinn et al. (2022). We take the log-space errors for dispersion and rotation speed in quadrature to get 0.11 dex (29%) for the velocity error (Figure 6, top panels). For the uncertainty of H I linewidths, we use 0.04 dex (9%), which is the average from Bradford et al. (2016). Adding the errors in quadrature gives a total velocity uncertainty of 0.10 dex (27% error), as shown in the bottom panel of Figure 6.

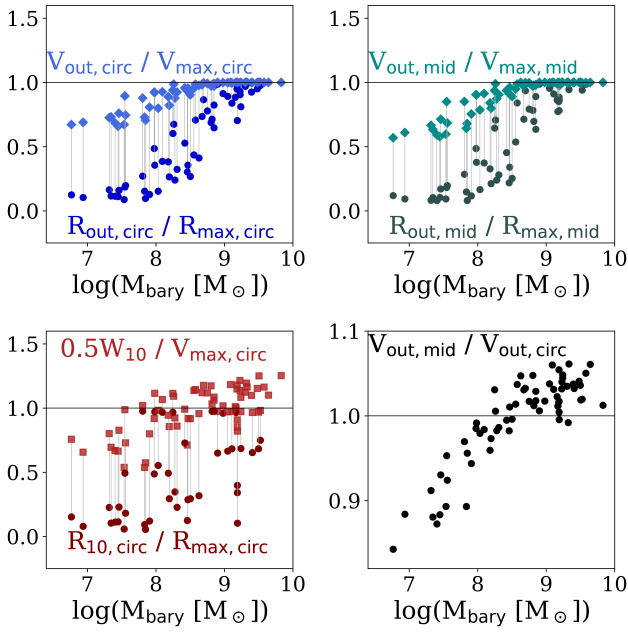


Figure 7. Velocity and radius ratios to compare each method to the maximum halo values as a function of baryonic mass. These panels correspond to the methods shown in Figure 6: upper left panel uses $V_{\text{out,circ}}$, upper right panel uses $V_{\text{out,mid}}$, and the bottom left panel uses W_{10} . The bottom right panel compares the spatially resolved H I velocities, and shows a galaxy mass dependence when using the midplane versus mass enclosed methods.

3.5 Comparing Velocity Methods and their Radial Extent

We examine the radial extent probed by each method in Figure 7. We plot ratios of the H I velocities and radii relative to the halo values as a function of baryonic mass.

The top row of Figure 7 shows how well the spatially resolved H I methods recover the maximum halo values, whether using the mass enclosed (top left panel) or midplane potential (top right panel). Both methods underpredict the maximum halo speed and corresponding radius by very similar factors at a given baryonic mass. With galaxies at $M_{\text{bary}} > 10^{8.5} M_{\odot}$, the H I size at the $1 M_{\odot} \text{ pc}^{-2}$ limit (R_1) extends to the flat part of the rotation curve. This is apparent with the velocity ratios being close to 1, while the corresponding radius can underestimate the $R_{\text{max,circ}}$ or $R_{\text{max,mid}}$ values with factors of $\sim 0.5 - 1.0$. At $M_{\text{bary}} < 10^{8.5} M_{\odot}$, the H I sizes shrink and limit the radial extent of spatially resolved rotation curves. R_1 moves interior to the rising part of the rotation curve, and the H I velocities significantly underpredict the halo speed. The velocity differences can be close to 50% for both the mass-enclosed and midplane methods.

The bottom right panel in Figure 7 demonstrates how the midplane and mass-enclosed H I velocities differ with baryonic mass. As stated earlier, if galaxies are in dynamic equilibrium and the assumption of spherical symmetry holds, the two methods should return the same velocity, but we find slight differences. At $\log(M_{\text{bary}}) < 8.2$, $V_{\text{out,mid}}$ systematically measures lower velocities than $V_{\text{out,circ}}$ with up to a 15% difference, while at higher masses, $V_{\text{out,mid}}$ measures higher velocities with up to a 6.2% difference. This trend is consistent with the dynamical expectation that a disk mass distribution, as found in the more massive dwarfs, will peak at a slightly higher velocity than a spherical distribution. Our lower-mass galaxies tend to be more prolate (see Keith et al. 2025), and will be more prone to disequilibrium due to feedback given their shallower potential wells.

These mass trends explain the velocity trend seen in the lower right panel.

In the bottom left panel of Figure 7, we compare the velocity and radius ratios for $W_{10}/2$. Technically, the unresolved H I linewidths are not set to a size extent of the measured HI, as the entire dwarf is usually detected within the single dish beam size. However, we define the corresponding (mass-enclosed) circular velocity as that which gives the same velocity as $W_{10}/2$. We find that this measures an equivalent radius that is comparable to the sizes from resolved rotation curves. Compared to the other H I linewidths, W_{10} is more sensitive to diffuse H I gas at larger radii and rotation speeds (Sardone et al. 2024). Given the Gaussian shape of the H I profile in dwarf galaxies, Sardone et al. (2024) found that W_{10} provides a larger velocity, closer to the maximum halo speed, though likely still an underestimate. In observations, W_{10} can be susceptible to noise and requires very deep and high signal-to-noise measurements. Here, we show our (noise-free) predictions for how W_{10} relates to $V_{\text{max,circ}}$. We find that W_{10} differs up to $\sim 47\%$. Compared to $V_{\text{out,circ}}$ and $V_{\text{out,mid}}$, W_{10} has more vertical scatter in its velocity ratios. Since we plot all H I linewidths with $i \approx 90^\circ$, this vertical scatter is likely not due to inclination, but it might be from diversity in H I profile shapes. Turbulent velocities have a non-negligible impact on H I linewidth shape, especially at lower galaxy masses (e.g., El-Badry et al. 2018). We will test the impact of dispersion on H I linewidths in future work.

In all methods, the velocity ratios and radius ratios decrease with lower baryonic masses. As galaxy mass decreases, H I velocities more significantly underestimate the maximum halo speed. A lower rotation speed is due to the fact that the H I radius shrinks and traces a smaller radius on the rotation curve, on the rising part. By comparing the velocity and radius ratios for the lowest mass galaxy in each panel of Figure 7, we can infer limiting factors for each method. For $V_{\text{out,circ}}$, we assume the same (mass-enclosed) gravitational potential for the H I rotation curve and halo speed, and therefore the main limiting factor must be the observable extent of the H I disk. The midplane method ($V_{\text{out,mid}}$) measures at the same radius, but gives a slightly lower velocity than $V_{\text{max,mid}}$ as mass decreases. This suggests that in addition to the H I size, $V_{\text{out,mid}}$ measurements also differ from $V_{\text{max,mid}}$ due to non-circular motions and dynamical disequilibrium. Lastly, as discussed above, W_{10} seems to be the most inaccurate tracer of the three presented in Figure 7, and it is not immediately clear why. We will explore the physical processes that set H I line profile shape in a future work.

3.6 bTFR with different H I sensitivity limits

Previously, we determined that our galaxies with $M_{\text{bary}} > 10^{8.5} M_{\odot}$ have canonical H I disk sizes which have reached the flat part of the rotation curve. However, the H I disk size is sensitive to the surface density limit that can be achieved by observations (e.g., Wang et al. 2025). So far we have used the H I limit of $\Sigma_{\text{out}} = 1 M_{\odot} \text{ pc}^{-2}$, which is the standard definition used in the literature. New and future H I surveys can push to deeper limits (as discussed in Section 4.2). In this section, we explore the sensitivities required to trace $R_{\text{max,mid}}$ and subsequently $V_{\text{max,mid}}$.

Figure 8 shows the H I column density profiles in three stellar mass bins for our simulated dwarf galaxies. Horizontal lines correspond to the H I surface density limits: 1.0, 0.08, 0.02, and $0.01 M_{\odot} \text{ pc}^{-2}$. Our column density profiles plateau with radius, but with different plateaus as a function of mass. More massive galaxies ($M_{\star} \gtrsim 10^8 M_{\odot}$) plateau around 10^{17} cm^{-2} , and less massive galaxies plateau around 10^{14} cm^{-2} . Our sample exhibits the full range of H I column densities found in other simulations ($10^{14} - 10^{21} \text{ cm}^{-2}$),

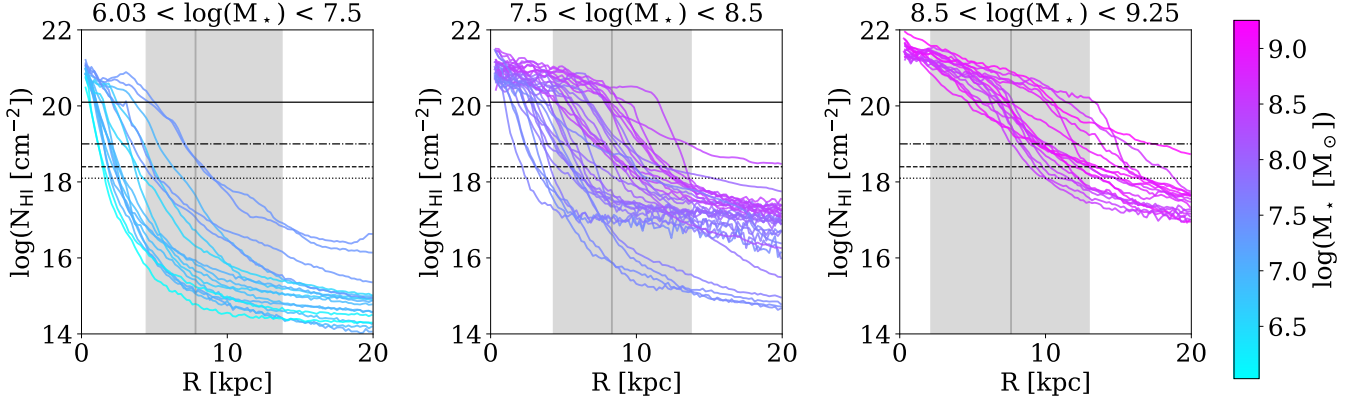


Figure 8. Column density profiles for three stellar mass bins. Each line is colored by its stellar mass, where lower masses are more blue and higher masses are more purple. The black horizontal lines correspond to the four surface density limits that we use for the bTFR: $1.0 \text{ M}_\odot \text{ pc}^{-2}$ ($1.25 \times 10^{20} \text{ cm}^{-2}$) is the solid line, $0.08 \text{ M}_\odot \text{ pc}^{-2}$ ($1 \times 10^{19} \text{ cm}^{-2}$) is the dotted-dashed line, $0.02 \text{ M}_\odot \text{ pc}^{-2}$ ($2.5 \times 10^{18} \text{ cm}^{-2}$) is the dashed line, and $0.01 \text{ M}_\odot \text{ pc}^{-2}$ ($1.25 \times 10^{18} \text{ cm}^{-2}$) is the dotted line. The shaded grey region shows the range of $R_{\text{max,circ}}$ values for the galaxies in that mass bin, and the vertical grey line shows the mean value. The higher mass bins (middle and right panels) exhibit column density profiles that plateau around 10^{17} cm^{-2} , while the lowest mass bin (left panel) has profiles that plateau around 10^{14} cm^{-2} .

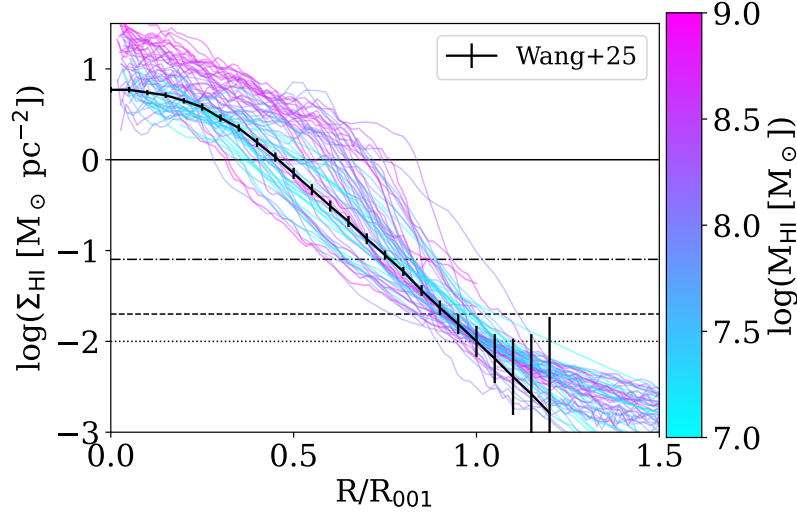


Figure 9. Comparison of H I surface density profiles from our simulated sample (colored by H I mass) versus the median profile of the FEASTS sample (Wang et al. 2025) (black curve). The horizontal lines represent the same surface density limits as Figure 8. The observed median profile is consistent with the range of our simulated profiles, though constraints at further radii are needed to confirm or rule out the more extended H I gas in our simulations.

in which the lower-density gas corresponds to cold accretion from the intergalactic medium (Kereš et al. 2005; Popping et al. 2009; Cook et al. 2024).

In Figure 9, we compare our surface density profiles to the median surface density profile for the FEASTS sample (Wang et al. 2025). This profile is normalized by R_{001} , which is the H I size at a surface density limit of $0.01 \text{ M}_\odot \text{ pc}^{-2}$. The FEASTS sample targets more massive galaxies, with $M_{\text{HI}} \gtrsim 10^{8.5} \text{ M}_\odot$ and $M_\star \gtrsim 10^{8.5} \text{ M}_\odot$, while most of our galaxies are below this mass range. Thus, it is not clear if this comparison is valid, but the normalized R/R_{001} span two orders of magnitude in galaxy mass and show uniformity, suggesting extrapolation to lower masses might be acceptable. With this caveat, we find that the observed median profile lies within the range of our simulated surface density profiles. It seems that the simulations might have larger H I extents compared to the observed

sample, though this interpretation appears to be at odds with the results shown in Figure 4. However, discrepancies may also be due to the feedback and radiative transfer models used in our simulations. For example, simulations have a hard time maintaining molecular gas, which wants to immediately form star particles, so must be regulated by feedback. Our higher H I surface densities in the central regions of galaxies are likely because some of this gas should be molecular, but feedback turns it to H I instead. Overall, it is clear that the simulations tend to follow the observational trend in normalized H I surface density profile at large radii. Additional observations of surface density profiles out to large radii like R_{001} will help us to calibrate the gas physics.

In Figure 10, we compare the bTFR using $V_{\text{out,mid}}$ at different surface density limits. As expected, for galaxies with $V_{\text{max}} < 70 \text{ km s}^{-1}$, the higher surface density of $2 \text{ M}_\odot \text{ pc}^{-2}$ (equivalent to

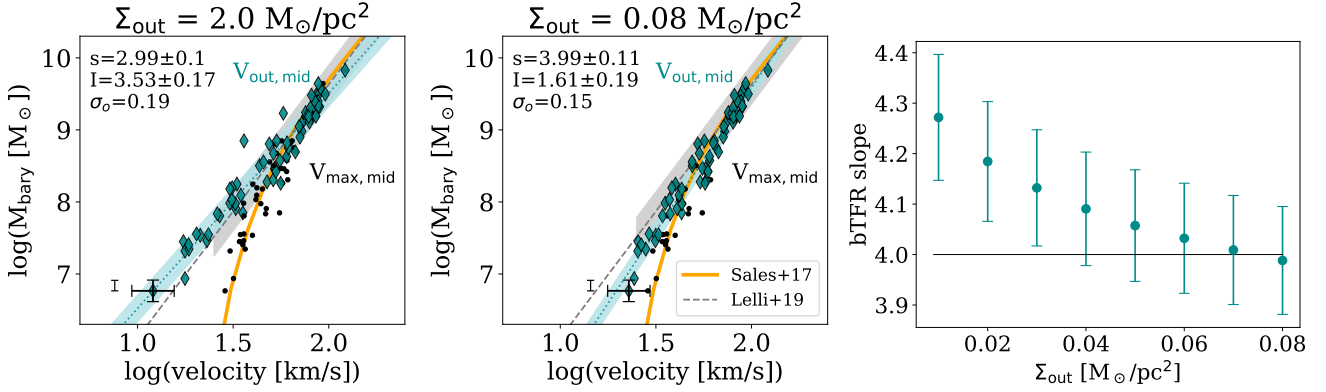


Figure 10. The bTFR using $V_{\text{out,mid}}$ (dark cyan points) and $V_{\text{max,mid}}$ (black points) with different H I sensitivity limits: left panel is $2 \text{ M}_{\odot} \text{ pc}^{-2}$ ($2.5 \times 10^{20} \text{ cm}^{-2}$) and the middle panel is $0.08 \text{ M}_{\odot} \text{ pc}^{-2}$ ($1 \times 10^{19} \text{ cm}^{-2}$). The dotted blue line shows a power-law fit to $V_{\text{out,mid}}$, and the shaded blue region represents the $1\text{-}\sigma$ vertical scatter. Improving the sensitivity limit to $< 0.08 \text{ M}_{\odot} \text{ pc}^{-2}$ measures far out enough in radius such that $V_{\text{out,mid}}$ is within error of $V_{\text{max,mid}}$, at least for our galaxy sample. Errors on the lowest-mass galaxy are the same as in Figure 6 (top panels). The right panel demonstrates how the bTFR slope is > 4 and steepens as the outer H I surface density limit improves from $0.08 \text{ M}_{\odot} \text{ pc}^{-2}$ to $0.01 \text{ M}_{\odot} \text{ pc}^{-2}$.

worse sensitivity) probes a radial extent that is interior to the radius corresponding to $1 \text{ M}_{\odot} \text{ pc}^{-2}$ (see Figure 8). Thus, the measured H I disk radius and rotation velocity both get smaller, because the velocity measurement moves inward on the rising part of the rotation curve. On the other hand, improving sensitivity and reaching a lower H I column density does indeed begin to close the gap between $V_{\text{out,mid}}$ and $V_{\text{max,mid}}$. At $0.08 \text{ M}_{\odot} \text{ pc}^{-2}$, $V_{\text{out,mid}}$ recovers $V_{\text{max,mid}}$ down to 45 km s^{-1} . This leads to a change in the bTFR slope as a function of H I surface density limit, which can be tested by observations. We fit one power-law slope for our sample of galaxies (with $V_{\text{max,mid}} = 28\text{--}122 \text{ km s}^{-1}$). For $0.08 \text{ M}_{\odot} \text{ pc}^{-2}$, the bTFR slope becomes steeper with a value of 3.99 ± 0.11 , and steeper still for $0.01 \text{ M}_{\odot} \text{ pc}^{-2}$ with a value of 4.27 ± 0.12 . As demonstrated by the lowest limits, a slope > 4.0 may indicate a turndown in the bTFR. Measuring the outermost rotation velocity at lower surface densities could allow us to recover the maximum halo speed, though sufficient spatial resolution is also needed. At a surface density limit of $0.01 \text{ M}_{\odot} \text{ pc}^{-2}$, our sample has H I sizes ranging from $1.6\text{--}20 \text{ kpc}$.

4 DISCUSSION

4.1 Non-circular motions and the bTFR

Although our spatially resolved bTFR slopes are generally consistent with observations (Table 1 and Section 3.3), we consider factors which could affect our rotation curve analysis.

Rotation curves measured in observations and simulations may not fully account for the non-circular motions of dwarf galaxies. Observers typically use software such as 3DBAROLO (Di Teodoro & Fraternali 2015) or FAT (Józsa et al. 2007; Kamphuis et al. 2015) to model rotation curves from emission spectra. These codes iteratively model the galaxy with tilted three-dimensional rings to match observed kinematic information, and free parameters such as inclination and position angle can be constrained. In our simulations, we measure rotation curves when using the mass enclosed by spherical shells or otherwise calculate the velocity based on the radial component of the gravitational acceleration of the entire galaxy on a few sample points in the midplane. Measuring rotation curves in observations or simulations require some assumptions for smoothness and symmetry, though not all galaxies have well-ordered, thin, gaseous rotating disks. A body of existing work suggests that deviations from this

ideal systematically act to reduce the rotation velocities compared to that measured by enclosed mass (e.g., Read et al. 2016; El-Badry et al. 2017; Verbeke et al. 2017; Pineda et al. 2017; Oman et al. 2019; Roper et al. 2023; Downing & Oman 2023; Sands et al. 2024), and that non-circular velocities become increasingly important as mass decreases (Marasco et al. 2018). The bursty star formation in dwarf galaxies can cause fluctuations in the gravitational potential that drive the galaxy out of equilibrium (e.g., Pontzen & Governato 2012), which can impact the rotation curve (Read et al. 2016). The feedback from these bursts drive non-circular motions such as turbulence or outflows, or the creation of H I holes that may not be discernible depending on the inclination angle of the observed galaxy (Read et al. 2016; Verbeke et al. 2017; Sands et al. 2024). Marasco et al. (2018) shows that triaxial halos can induce bars (radial gas flows) in dwarf galaxies, and the majority of our simulated galaxies with $M_{\star} < 10^8 \text{ M}_{\odot}$ reside in triaxial halos (Keith et al. 2025). Gas can also experience pressure support that reduces the velocity relative to stars and dark matter, and the pressure support may come from thermal, magnetic, or cosmic ray pressure (Sands et al. 2024). Thermal pressure support is generally thought to be most relevant in the central regions (Pineda et al. 2017), but effects from pressure support may uniquely influence the H I size and mass in lower mass galaxies. Disk thickness also plays an increasingly important role as mass decreases (Mancera Piña et al. 2022) since disks become thicker with decreasing mass (e.g., Sánchez-Janssen et al. 2010; Roychowdhury et al. 2013), and this can cause overlapping velocities between modeled thin rings. Most of these effects tend to lower the observed rotation velocity further than what we measure with either of our mass enclosed or midplane potential methods.

This uncertainty is why dwarf galaxies are often selected to be well-behaved before being included in velocity studies. Previous modelers have suggested that a galaxy’s disk may be out of equilibrium if the H I line-of-sight velocity dispersion is $> 20 \text{ km s}^{-1}$ (Verbeke et al. 2017), or not well modeled if the disk height-to-radius ratio is > 0.3 (Sands et al. 2024) or inclination is $< 40^\circ$ (Read et al. 2016). However, it has been found that discarding galaxies that are not well-behaved leads to a steeper bTFR slope (e.g., Stark et al. 2009; Downing & Oman 2023). As previously mentioned, we have chosen to use all of our galaxies despite their morphology, which may explain discrepancies between our bTFR results and that of observations. In addition to this, it is likely that our bTFR slope would change

if we were able to measure the rotation speeds with non-circular motions fully taken into account. We already see this in the $V_{\text{out,mid}}$ bTFR result, where measuring the rotation speed with the midplane potential gives a lower velocity than using the enclosed mass, presumably due to increasing importance of non-circular motions, and gives a slope of 3.36 instead of 3.69.

4.2 Can we measure V_{max} in dwarf galaxies with future observations?

Measuring V_{max} for dwarf galaxies with spatially resolved observations will first require a larger sample with sufficiently low rotation speeds. Similar to ALFALFA, the WALLABY, FASHI (FAST all sky H I survey; Zhang et al. 2024), and CRAFTS (Commensal Radio Astronomy FasT Survey; Zhang et al. 2021) surveys will be the next deep, wide-field H I surveys to discover many more galaxies. WALLABY is expected to cover 14000 deg² (Duffy et al. 2012; Murugesan et al. 2024), while FASHI and CRAFTS will cover ~ 22000 deg² (Zhang et al. 2021, 2024), and each survey is expected to detect $\sim 10^5$ galaxies. WALLABY will cover a portion of the southern sky, in the declination range $-60^\circ < \delta < -15^\circ$ (Murugesan et al. 2024), while other surveys will cover portions of the northern sky, like FASHI/CRAFTS with declinations $-14^\circ < \delta < +66^\circ$ (Zhang et al. 2021, 2024) and Apertif with $+30^\circ < \delta < +60^\circ$ (Adams et al. 2022). In addition to observing more galaxies with large sky coverage, MIGHTEE-H I (Maddox et al. 2021) will cover a deeper cosmological volume up to redshift of 0.6. Combining these surveys to identify lower-mass galaxies and conduct follow-up for the kinematics could yield a decent sample of dwarf galaxies to study the bTFR. The WALLABY pilot survey already measured the bTFR for 61 galaxies down to rotation speeds ~ 35 km s⁻¹ (Deg et al. 2024), but no turndown was detected. However, it is also worth noting that their sample does not include any galaxies with $M_{\text{bary}} < 10^8 M_\odot$, which is the regime where we predict a turndown, and they used an H I surface density limit of $1 M_\odot \text{ pc}^{-2}$.

Furthermore, to measure V_{max} in dwarf galaxies with spatially resolved observations, we need sufficiently low H I surface density limits. Our results suggest that solely observing galaxies at low rotation speeds is not enough to observe a turndown in the bTFR if we use the $1 M_\odot \text{ pc}^{-2}$ surface density limit. Instead, measuring the rotation of diffuse H I gas at low densities is crucial. Figure 10 demonstrates that better sensitivity with a limit $\lesssim 0.08 M_\odot \text{ pc}^{-2}$ is needed to possibly measure the bTFR turndown with H I. Surveys like MHONGOOSE (de Blok et al. 2024) and FEASTS (Wang et al. 2025) focus on measuring the diffuse H I gas in the outskirts of galaxies, down to surface densities $\sim 0.0039 M_\odot \text{ pc}^{-2}$. MHONGOOSE has a sample of 30 galaxies, and FEASTS is designed to study 118 galaxies³, both with $M_{\text{HI}} \gtrsim 10^7 M_\odot$. Although MHONGOOSE and FEASTS have a limited sample of dwarf galaxies, V_{max} could be successfully measured. Going deeper with MIGHTEE-H I or surveys with the Square Kilometer Array - Mid (Swart et al. 2022) could also increase the sample of galaxies with kinematic information beyond the $1 M_\odot \text{ pc}^{-2}$ limit. If future H I surveys measure V_{out} for more dwarf galaxies at deeper sensitivities and find a steeper bTFR slope (> 4), this may confirm a turndown. Observing a turndown in the bTFR would provide evidence that indeed, the inefficient galaxy formation of lower-mass galaxies alters the scaling between an H I disk and dark matter halo, and would suggest that it is not the same in all mass regimes.

Lastly, from Figure 6, it is not clear that it is possible to measure V_{max} using unresolved H I linewidths, as even W_{10} shows little evidence for a turndown. Certainly the bTFR slope steepens as we move from a measurement at W_{20} to W_{10} (Table 1). Yet even with decent spectral resolution (2.6 km s^{-1}) and no observational noise, V_{max} is not within error of W_{10} for our simulated galaxies at $M_{\text{bary}} \lesssim 10^{8.5} M_\odot$. This result is in striking contrast to the general wisdom that unresolved linewidths will be necessary to obtain statistics at low masses. Instead, these results suggest we might have to rely on a handful of well-measured resolved velocities at low galaxy masses in order to probe for evidence of a bTFR turndown.

5 CONCLUSIONS

We analyze the bTFR for a sample of 66 simulated dwarf galaxies from the Marvel-ous and Marvelous Massive Dwarfs simulations. These galaxies span a mass range of $M_\star = 10^6 - 10^9 M_\odot$. They are primarily gas-dominated (Figure 1) and follow observed scaling relations for H I gas content and velocity widths (Figures 4 and 5).

Like previous galaxy simulations with CDM (e.g., Ferrero et al. 2012; Sales et al. 2017), we predict a turndown in the bTFR when the true maximum rotation velocity of the halo is measured (black points, Figure 6). The bTFR turndown occurs at $M_{\text{bary}} \lesssim 10^{8.5} M_\odot$, or a corresponding rotation speed $\lesssim 50 \text{ km s}^{-1}$. However, we determine the rotation velocity in other ways, including measuring within the outermost H I radius (at $1 M_\odot \text{ pc}^{-2}$) using the mass enclosed in spherical shells ($V_{\text{out,circ}}$), the gravitational potential in the midplane of the galaxy ($V_{\text{out,mid}}$), and various widths of the unresolved H I line profile (W_{50} , W_{20} , W_{10}). We find that none of these more observationally-oriented velocity measurements can recover the underlying turndown in the bTFR.

There are a few physical reasons why spatially resolved velocities might not trace the true $V_{\text{max,circ}}$ of the halo. We summarize two key findings:

- Spatially resolved velocities (at the $1 M_\odot \text{ pc}^{-2}$ limit) fail to trace V_{max} below $M_{\text{bary}} \sim 10^{8.5} M_\odot$ (Figure 6) because the size of the H I disk shrinks as mass declines (see Figure 7). As the disk shrinks, the velocity is measured further in on the rising part of the rotation curve, reducing the outermost measured velocity.
- Our H I column density profiles predict that more gas can be observed past the fiducial limit of $1 M_\odot \text{ pc}^{-2}$ (Figure 8), though more observations are needed to confirm the extended H I at radii beyond the $0.01 M_\odot \text{ pc}^{-2}$ limit (Figure 9). Better sensitivity is necessary to observe the more diffuse gas. We predict that a turndown in the bTFR (detectable as a slope > 4) could be measured using $V_{\text{out,mid}}$ if an H I sensitivity limit of $\lesssim 0.08 M_\odot \text{ pc}^{-2}$ is achieved (Figure 10). This sensitivity is within reach of measurements in MIGHTEE-HI, MHONGOOSE, and FEASTS, though the number of observed dwarf galaxies that reach this depth may be small overall.

It is notable that our W_{20} unresolved H I linewidths are not sensitive to a bTFR turndown, and instead continue the power-law trend from higher mass galaxies. A steeper slope might be recoverable if W_{10} is measured, but this requires incredibly deep integrations with high signal-to-noise (Sardone et al. 2024), and will be difficult to achieve for more dwarf galaxies. It is generally assumed that unresolved H I linewidths must be used in order to obtain statistical samples of H I velocities at the dwarf scale. However, our results suggest that fewer dwarfs but with resolved rotation curves to lower H I surface densities might be the only way to observationally recover a turndown in the bTFR.

³ <https://github.com/FEASTS/LVgal/wiki>

ACKNOWLEDGEMENTS

Resources supporting this work were provided by the NASA High-End Computing (HEC) Program through the NASA Advanced Supercomputing (NAS) Division at Ames Research Center. Some of the simulations were performed using resources made available by the Flatiron Institute. The Flatiron Institute is a division of the Simons Foundation. This work used Stampede2 at the Texas Advanced Computing Center (TACC) through allocation MCA94P018 from the Advanced Cyberinfrastructure Coordination Ecosystem: Services & Support (ACCESS) program, which is supported by U.S. National Science Foundation grants #2138259, #2138286, #2138307, #2137603, and #2138296. A.H.G.P. is supported by NSF Grant No. AST-2008110. J.W. is supported by a grant from NSERC (National Science and Engineering Research Council) Canada.

REFERENCES

- Abel T., Anninos P., Zhang Y., Norman M. L., 1997, *New A*, **2**, 181
- Adams E. A. K., et al., 2022, *A&A*, **667**, A38
- Arnett D., 1996, *Supernovae and Nucleosynthesis: An Investigation of the History of Matter from the Big Bang to the Present*
- Azartash-Namin B., et al., 2024, *ApJ*, **970**, 40
- Barnes J., Efstathiou G., 1987, *ApJ*, **319**, 575
- Behroozi P. S., Wechsler R. H., Conroy C., 2013, *ApJ*, **770**, 57
- Black J. H., 1981, *MNRAS*, **197**, 553
- Bosma A., 1978, PhD thesis, University of Groningen, Netherlands
- Bradford J. D., Geha M. C., Blanton M. R., 2015, *ApJ*, **809**, 146
- Bradford J. D., Geha M. C., van den Bosch F. C., 2016, *ApJ*, **832**, 11
- Broeils A. H., Rhee M. H., 1997, *A&A*, **324**, 877
- Brook C. B., Shankar F., 2016, *MNRAS*, **455**, 3841
- Brook C. B., Santos-Santos I., Stinson G., 2016, *MNRAS*, **459**, 638
- Brooks A. M., Papastergis E., Christensen C. R., Governato F., Stilp A., Quinn T. R., Wadsley J., 2017, *ApJ*, **850**, 97
- Catinella B., et al., 2010, *MNRAS*, **403**, 683
- Cen R., 1992, *ApJS*, **78**, 341
- Christensen C., Quinn T., Governato F., Stilp A., Shen S., Wadsley J., 2012, *MNRAS*, **425**, 3058
- Cook A. W. S., van de Voort F., Pakmor R., Grand R. J. J., 2024, *arXiv e-prints*, p. [arXiv:2409.05578](#)
- Cowie L. L., McKee C. F., 1977, *ApJ*, **211**, 135
- Deg N., et al., 2024, *ApJ*, **976**, 159
- Di Cintio A., Brook C. B., Macciò A. V., Stinson G. S., Knebe A., Dutton A. A., Wadsley J., 2014, *MNRAS*, **437**, 415
- Di Teodoro E. M., Fraternali F., 2015, *MNRAS*, **451**, 3021
- Downing E. R., Oman K. A., 2023, *MNRAS*, **522**, 3318
- Duffy A. R., Meyer M. J., Staveley-Smith L., Bernyk M., Croton D. J., Koribalski B. S., Gerstmann D., Westerlund S., 2012, *MNRAS*, **426**, 3385
- Dutton A. A., 2012, *MNRAS*, **424**, 3123
- Dutton A. A., Obreja A., Macciò A. V., 2019, *MNRAS*, **482**, 5606
- El-Badry K., Wetzel A. R., Geha M., Quataert E., Hopkins P. F., Kereš D., Chan T. K., Faucher-Giguère C.-A., 2017, *ApJ*, **835**, 193
- El-Badry K., et al., 2018, *MNRAS*, **477**, 1536
- Ferrero I., Abadi M. G., Navarro J. F., Sales L. V., Gurovich S., 2012, *MNRAS*, **425**, 2817
- Geha M., Blanton M. R., Masjedi M., West A. A., 2006, *ApJ*, **653**, 240
- Gill S. P. D., Knebe A., Gibson B. K., 2004, *MNRAS*, **351**, 399
- Girardi L., et al., 2010, *ApJ*, **724**, 1030
- Haardt F., Madau P., 2012, *ApJ*, **746**, 125
- Haynes M. P., et al., 2011, *AJ*, **142**, 170
- Haynes M. P., et al., 2018, *ApJ*, **861**, 49
- Hunter D. A., Elmegreen B. G., Gehret E., 2016, *AJ*, **151**, 136
- Józsa G. I. G., Kenn F., Klein U., Oosterloo T. A., 2007, *A&A*, **468**, 731
- Kalé L., Krishnan S., 1993, in Paepcke A., ed., *Proceedings of OOPSLA'93*. ACM Press, pp 91–108
- Kamphuis P., Józsa G. I. G., Oh S. H., Spekkens K., Urbancic N., Serra P., Koribalski B. S., Dettmar R. J., 2015, *MNRAS*, **452**, 3139
- Keith B., et al., 2025, *arXiv e-prints*, p. [arXiv:2501.16317](#)
- Keller B. W., Wadsley J., Benincasa S. M., Couchman H. M. P., 2014, *MNRAS*, **442**, 3013
- Kereš D., Katz N., Weinberg D. H., Davé R., 2005, *MNRAS*, **363**, 2
- Klypin A., Karachentsev I., Makarov D., Nasonova O., 2015, *MNRAS*, **454**, 1798
- Knollmann S. R., Knebe A., 2009, *ApJS*, **182**, 608
- Koribalski B. S., et al., 2020, *Ap&SS*, **365**, 118
- Kroupa P., 2001, *MNRAS*, **322**, 231
- Krumm N., Burstein D., 1984, *AJ*, **89**, 1319
- Lelli F., McGaugh S. S., Schombert J. M., 2016a, *AJ*, **152**, 157
- Lelli F., McGaugh S. S., Schombert J. M., 2016b, *ApJ*, **816**, L14
- Lelli F., McGaugh S. S., Schombert J. M., Desmond H., Katz H., 2019, *MNRAS*, **484**, 3267
- Macciò A. V., Udrescu S. M., Dutton A. A., Obreja A., Wang L., Stinson G. R., Kang X., 2016, *MNRAS*, **463**, L69
- Maddox N., et al., 2021, *A&A*, **646**, A35
- Mancera Piña P. E., Fraternali F., Oosterloo T., Adams E. A. K., di Teodoro E., Bacchini C., Iorio G., 2022, *MNRAS*, **514**, 3329
- Marasco A., Oman K. A., Navarro J. F., Frenk C. S., Oosterloo T., 2018, *MNRAS*, **476**, 2168
- Marigo P., Girardi L., Bressan A., Groenewegen M. A. T., Silva L., Granato G. L., 2008, *A&A*, **482**, 883
- McGaugh S. S., Schombert J. M., 2014, *AJ*, **148**, 77
- McGaugh S. S., Schombert J. M., Bothun G. D., de Blok W. J. G., 2000, *ApJ*, **533**, L99
- McQuinn K. B. W., et al., 2022, *ApJ*, **940**, 8
- Meidt S. E., et al., 2014, *ApJ*, **788**, 144
- Menon H., Wesolowski L., Zheng G., Jetley P., Kale L., Quinn T., Governato F., 2015, *Computational Astrophysics and Cosmology*, **2**, 1
- Moster B. P., Naab T., White S. D. M., 2013, *MNRAS*, **428**, 3121
- Munshi F., et al., 2013, *ApJ*, **766**, 56
- Munshi F., Brooks A. M., Applebaum E., Christensen C. R., Quinn T., Sligh S., 2021, *ApJ*, **923**, 35
- Murugesan C., et al., 2024, *PASA*, **41**, e088
- Oh S.-H., et al., 2015, *AJ*, **149**, 180
- Oman K. A., Navarro J. F., Sales L. V., Fattahi A., Frenk C. S., Sawala T., Schaller M., White S. D. M., 2016, *MNRAS*, **460**, 3610
- Oman K. A., Marasco A., Navarro J. F., Frenk C. S., Schaye J., Benítez-Llambay A., 2019, *MNRAS*, **482**, 821
- Ostriker J. P., McKee C. F., 1988, *Reviews of Modern Physics*, **60**, 1
- Papastergis E., Shankar F., 2016, *A&A*, **591**, A58
- Peebles P. J. E., 1969, *ApJ*, **155**, 393
- Pineda J. C. B., Hayward C. C., Springel V., Mendes de Oliveira C., 2017, *MNRAS*, **466**, 63
- Planck Collaboration et al., 2016, *A&A*, **594**, A13
- Planck Collaboration et al., 2020, *A&A*, **641**, A6
- Pontzen A., Governato F., 2012, *MNRAS*, **421**, 3464
- Pontzen A., Roškar R., Stinson G., Woods R., 2013, pynbody: N-Body/SPH analysis for python, Astrophysics Source Code Library, record ascl:1305.002
- Popping A., Davé R., Braun R., Oppenheimer B. D., 2009, *A&A*, **504**, 15
- Power C., Navarro J. F., Jenkins A., Frenk C. S., White S. D. M., Springel V., Stadel J., Quinn T., 2003, *MNRAS*, **338**, 14
- Read J. I., Iorio G., Agertz O., Fraternali F., 2016, *MNRAS*, **462**, 3628
- Read J. I., Iorio G., Agertz O., Fraternali F., 2017, *MNRAS*, **467**, 2019
- Roper F. A., Oman K. A., Frenk C. S., Benítez-Llambay A., Navarro J. F., Santos-Santos I. M. E., 2023, *MNRAS*, **521**, 1316
- Roychowdhury S., Chengalur J. N., Karachentsev I. D., Kaisina E. I., 2013, *MNRAS*, **436**, L104
- Rubin V. C., Ford Jr. W. K., Thonnard N., 1980, *Astrophysical Journal*, **238**, 471
- Sales L. V., et al., 2017, *MNRAS*, **464**, 2419
- Sánchez-Janssen R., Méndez-Abreu J., Aguerri J. A. L., 2010, *MNRAS*, **406**, L65
- Sands I. S., et al., 2024, *arXiv e-prints*, p. [arXiv:2404.16247](#)

- Sardone A., Peter A. H. G., Brooks A. M., Kaczmarek J., 2024, [ApJ](#), **964**, 135
- Shen S., Wadsley J., Stinson G., 2010, [MNRAS](#), **407**, 1581
- Spekkens K., Lewis C., Deg N., 2020, in American Astronomical Society Meeting Abstracts #236. p. 109.05
- Spergel D. N., et al., 2007, [ApJS](#), **170**, 377
- Stark D. V., McGaugh S. S., Swaters R. A., 2009, [AJ](#), **138**, 392
- Stevens A. R. H., Diemer B., Lagos C. d. P., Nelson D., Obreschkow D., Wang J., Marinacci F., 2019, [MNRAS](#), **490**, 96
- Stilp A. M., Dalcanton J. J., Warren S. R., Skillman E., Ott J., Koribalski B., 2013a, [ApJ](#), **765**, 136
- Stilp A. M., Dalcanton J. J., Skillman E., Warren S. R., Ott J., Koribalski B., 2013b, [ApJ](#), **773**, 88
- Stinson G., Seth A., Katz N., Wadsley J., Governato F., Quinn T., 2006, [MNRAS](#), **373**, 1074
- Swart G. P., Dewdney P. E., Cremonini A., 2022, [Journal of Astronomical Telescopes, Instruments, and Systems](#), **8**, 011021
- Tamburro D., Rix H. W., Leroy A. K., Mac Low M. M., Walter F., Kennicutt R. C., Brinks E., de Blok W. J. G., 2009, [AJ](#), **137**, 4424
- Tremmel M., Karcher M., Governato F., Volonteri M., Quinn T. R., Pontzen A., Anderson L., Bellovary J., 2017, [MNRAS](#), **470**, 1121
- Trujillo-Gomez S., Schneider A., Papastergis E., Reed D. S., Lake G., 2018, [MNRAS](#), **475**, 4825
- Tully R. B., Fisher J. R., 1977, [A&A](#), **54**, 661
- Verbeke R., Papastergis E., Ponomareva A. A., Rathi S., De Rijcke S., 2017, [A&A](#), **607**, A13
- Verheijen M. A. W., 2001, [ApJ](#), **563**, 694
- Verner D. A., Ferland G. J., 1996, [ApJS](#), **103**, 467
- Wadsley J. W., Stadel J., Quinn T., 2004, [New A](#), **9**, 137
- Wadsley J. W., Keller B. W., Quinn T. R., 2017, [MNRAS](#), **471**, 2357
- Wang J., Koribalski B. S., Serra P., van der Hulst T., Roychowdhury S., Kamphuis P., Chengalur J. N., 2016, [MNRAS](#), **460**, 2143
- Wang J., et al., 2025, [ApJ](#), **980**, 25
- Wechsler R. H., Tinker J. L., 2018, [ARA&A](#), **56**, 435
- Yaryura C. Y., Helmi A., Abadi M. G., Starkenburg E., 2016, [MNRAS](#), **457**, 2415
- Zhang K., et al., 2021, [MNRAS](#), **500**, 1741
- Zhang C.-P., et al., 2024, [Science China Physics, Mechanics, and Astronomy](#), **67**, 219511
- Zhu Y.-N., Wu H., Li H.-N., Cao C., 2010, [Research in Astronomy and Astrophysics](#), **10**, 329
- de Blok W. J. G., et al., 2024, [A&A](#), **688**, A109
- Šiljeg B., et al., 2024, [arXiv e-prints](#), p. arXiv:2409.18825
- van Cappellen W. A., et al., 2022, [A&A](#), **658**, A146

This paper has been typeset from a \LaTeX file prepared by the author.